Pergamon

0967-0637(95)00035-6

Deep-Sea Research I, Vol. 42, No. 8, pp. 1359–1398, 1995

0967-0637/95 $9.50 + 0.00

Coupled physical and biological modelling of the spring bloom in the North Atlantic (II): three dimensional bloom and post-bloom processes

D. J. McGILLICUDDY Jr,* A. R. ROBINSON*
and J. J. McCARTHY*

(*Received* 31 *March* 1994, *in revised form* 9 *September* 1994, *accepted* 12 *January* 1995)

Abstract—A set of three dimensional coupled physical and biological models is used to ascertain the importance of mesoscale dynamical activity during the 1989 JGOFS North Atlantic Bloom Experiment. First, various physical processes causing nutrient flux are studied with a simplified one compartment "nutrient model" utilized in an isolated vortex. A hierarchy of vertical transport processes is described for this case, ranging from the relatively minor fluxes caused by vortex stretching in the interior to the moderate transport resulting from the interaction of the interior and wind driven motions to the rather vigorous (3 m per day) effective transport caused by the propagation of the vortex. With these flux mechanisms in hand, the tuned four compartment biological model described in Part 1 is used to simulate the Small eddy in isolation. Together the propagation flux and the lifting of density surfaces caused by vortex evolution result in a twofold increase in mixed layer nitrate over that predicted by a one dimensional model. Enhanced phytoplankton and heterotroph production is associated with the elevated nutrient concentrations. Finally the three eddy configuration observed during the experiment is simulated. While all the previous vertical transports are active in this case, they are overshadowed by intense vertical motions associated with eddy–eddy interactions. Nutrient enhancements of up to an order of magnitude occur in the simulations that substantially increase both plant and animal production in localized regions for periods of weeks.

1. INTRODUCTION

Physical, biological and chemical properties of the open ocean vary a great deal on many spatial and temporal scales. In order to understand the observed distributions it is necessary to deal realistically and explicitly with the mechanisms responsible for this variability. In general this requires that the dynamical evolution of four dimensional oceanic fields be understood; it is essential to view observations in their spatial and temporal context. Interdisciplinary model systems are a natural media for such analysis. The assimilation of data forces the model to agree with observations to within prescribed error bounds, while providing space–time continuous fields consistent with the model dynamics. The resulting optimal field estimates serve as an ideal framework for process investigations. This approach has been used in the present study and a companion paper (McGillicuddy *et al.*, 1995) (hereafter MMR95) to examine the 1989 JGOFS North Atlantic Bloom data set.

*Department of Earth and Planetary Sciences, Harvard University, Cambridge, MA 02138, U.S.A.; present address: Woods Hole Oceanographic Institution, Woods Hole, MA 02543, U.S.A.

The fact that open ocean phytoplankton live in a highly dynamic environment shapes their ecology in two basic ways. First, ocean circulation can affect primary productivity by modulating *in situ* growth rates. Second, the distribution of biogenic material is continually deformed and rearranged through transport and advective processes. Let us begin with the rates of local production. In the open ocean, the growth of phytoplankton is limited primarily by either light or the availability of inorganic nutrients (most notably nitrogen). Thus, any physical process that affects the concentration of nutrient in or the solar radiation incident upon a water parcel can potentially influence the rate of photosynthesis within it.

In general, the fluid medium in which open ocean phytoplankton are immersed can be broken down into two distinct, yet interconnected, physical regimes. Typically there is a vertically well mixed surface layer of tens to sometimes hundreds of meters where the physical, biological and chemical constituents are homogeneously distributed by turbulent processes. Below this layer lie deep oceanic flow fields that are dominated by mesoscale motions with characteristic lateral extents of tens to hundreds of kilometers and time scales of several days to months. The currents, fronts and eddies that make up these deep fields are approximately in geostrophic balance and their dynamics are governed by the conservation of potential vorticity.

Both of these regimes contain a variety of mechanisms capable of regulating growth rates. In the surface boundary layer, vertical mixing from either direct wind forcing or buoyant convection can act to entrain nutrients from below into the often nutrient depleted near surface region. The extent of vertical mixing also influences the amount of the light that phytoplankton are exposed to. Sverdrup's (1953) conceptual model of a light limited phytoplankton population is useful in understanding some aspects of this issue. He noted the existence of a critical mixing depth at which the average light intensity was just sufficient to compensate for integrated respiratory losses. Only when the depth of mixing is shallower than the critical depth can the population sustain net growth. Thus, the vertical extent of the mixed layer in relation to the ambient light field is of crucial importance.

Mesoscale flows influence primary productivity primarily through their effect on nutrient availability. Vertical perturbations of the density surfaces in the main thermocline associated with mesoscale currents often extend into the upper ocean and increase or decrease nutrient concentrations accordingly. The dynamics of these features can produce vertical motions that transport nutrients into the euphotic zone. For example, it has been shown that the relaxation of the depressed density surfaces of an anticyclonic vortex during frictional decay can cause upwelling sufficient to produce a measurable increase in plant biomass in the interior of the feature (Nelson *et al.*, 1989; Franks *et al.*, 1986). The vorticity dynamics of mesoscale flows can also induce significant vertical velocity through the process of vortex stretching. Woods (1988) has proposed this as the main mechanism by which ocean eddies influence primary productivity. Conservation of potential vorticity demands that local changes in relative vorticity be balanced by adjustment of the depth of a fluid layer, therefore resulting in either upwelling or downwelling. Mesoscale dynamical processes, such as the meandering of a thin jet, produce submesoscale "hotspots" of locally intense vertical motion. Strass (1992) has analyzed high resolution vertical sections of density and chlorophyll in the North Atlantic and identified a peak in the variance spectrum of chlorophyll at approximately 10 km which appears consistent with biomass accumulations caused by submesoscale upwelling at fronts. These spatially and temporally intermittent events are phenomenologically distinct from submesoscale lenses. Results

from numerical models indicate rates of vertical motions ranging from several to tens of meters per day. A combination of observations and analysis in frontal regions has suggested vertical velocities as high as 40 m per day (Pollard and Regier, 1992) arise from ageostrophic advections of the vorticity field.

Surface boundary layer and interior processes are not only relevant to primary production in their own right; the interaction between the two can also play an important role in determining the growth rate of phytoplankton. Klein and Hua (1988) showed how the combination of the wind driven and mesoscale flows can result in significant heterogeneity in the mixing layer depth field. The interaction between the deep ocean and the surface boundary layer can also induce significant vertical transport. Stevenson (1980) showed how the advection of the interior vorticity field by the wind driven surface current can result in vortex stretching comparable in magnitude to that caused by the interior dynamics alone.

Clearly, then, there is a wealth of physical processes that can strongly influence local rates of primary production. However, in order to understand fully the spatial and temporal variability of observed biological parameters, it is necessary to consider these processes as occurring within a dynamic fluid medium. Ocean currents continually rearrange biological fields of interest by advection, often resulting in complex and convoluted structures. The flow can transport biogenic material over considerable distances to regions quite different in nature from their area of formation (Angel and Fasham, 1983).

Coupled three dimensional physical and biological models have thus become an important tool in the analysis of biogeochemical variability. Sarmiento *et al.* (1993) have embedded Fasham *et al.*'s (1990) upper ocean ecosystem into a model of the North Atlantic general circulation. This approach facilitates the study of basin scale patterns of nitrogen cycling and plankton dynamics, but leaves mesoscale variability unresolved. Flierl and Davis (1993) have developed process oriented models capable of simulating the effects of mesoscale motions on biological and chemical distributions and have applied them in the Gulf Stream region. Using a contour dynamics method to simulate a quasigeostrophic thin jet with a simple mixed layer model attached at the surface, the authors examine the effects of Gulf Stream meandering on a nutrient–phytoplankton–zooplankton ecosystem. Such an approach is quite useful for examining the basic processes by which the physics of the system affects biological distributions. However, direct comparisons with observations are made difficult by the idealized nature of the physical and biological formulation of the problem.

The main focus of the present effort is to make direct contact between models and data in the study of how mesoscale and upper ocean dynamics affect primary productivity and its variability. The approach is to incorporate biological components into regional numerical models of open ocean physics that are capable of producing realistic representations of oceanic flow fields. The ability to handle open boundary conditions in these physical models has made it possible to represent adequately very energetic mesoscale phenomena on the appropriate space and time scales (Robinson and Walstad, 1987; Robinson, 1993). Such models can be initialized with real ocean data and periodically updated via data assimilation to produce optimal four dimensional field estimates that are consistent with the available data and dynamically interpolated across data sparse regions. The resulting fields provide an ideal setting for the simulation of biogeochemical and ecosystem dynamics in that the structures and variabilities are representative of the real

ocean. This provides a framework for the investigation of coupled physical–biological processes that is firmly grounded in data.

In MMR95 such an interdisciplinary model system was introduced. It consists of a coupled quasigeostrophic and surface boundary layer physical model together with a four compartment (nitrate, phytoplankton, heterotroph and ammonium) nitrogen based biological model. A one dimensional implementation of the system was used to examine some aspects of the 1989 JGOFS North Atlantic Bloom data set. Two parallel simulations carried out inside and outside the Small eddy were shown to represent the general features of the two time series taken in these locations reasonably well. Thus, the model system has been tuned to the bloom data in one dimension. Although mesoscale *heterogeneity* was treated within the one dimensional framework, mesoscale *dynamical processes* were not. In this sense the tuning of the model is potentially incomplete; sources and sinks arising from mesoscale dynamical processes were not treated in the MMR95 one dimensional analysis. In this paper the full three dimensional physical–biological model will be used to study how mesoscale and upper ocean dynamical processes affect biological and chemical fields.

Because so many physical–biological processes are simultaneously active in complex models such as these, the behavior of the model can often be difficult to diagnose and understand. This analysis will therefore begin with the study of physical transport processes in a simplified "nutrient model". Nitrate is treated as a passive tracer in the three dimensional physical model and the net effect of biological processes is parameterized as instantaneous export of all nitrate that makes its way into the mixed layer. This exercise is useful in contrasting and quantifying the various physical mechanisms responsible for nutrient flux.

With these processes in hand the full biological model is then used to study mesoscale dynamical effects during and after the bloom. Surface fluxes derived from an operational atmospheric model are used to force the interdisciplinary model when shipboard observations are not available. This allows the simulations to be extended well into the "post-bloom" period. First, the Small eddy is studied in isolation and then the three eddy case is examined. Comparison with the one dimensional results is used to quantify the three dimensional effects.

2. THE INTERDISCIPLINARY MODEL SYSTEM

The coupled physical and biological models are described in detail in MMR95. The biological model is based on nitrogen and includes nitrate, phytoplankton, heterotroph and ammonium constituents. Phytoplankton growth is both light and nutrient limited, with ammonium being taken up preferentially. Heterotrophic consumption is based on the Ivlev grazing formulation. Nutrient regeneration to ammonium and export by heterotrophs includes both linear and quadratic terms to parameterize loss to higher trophic levels.

The biological quantities are incorporated as passive tracers in a coupled quasigeostrophic and surface boundary layer model. The evolution of a given scalar is given by the following equation for its interior and boundary layer components Φ and ϕ, respectively:

$$\phi_t + \alpha(J(\psi^*,\phi) + \mu(\Phi_x + \phi_x) + \nu(\Phi_y + \phi_y) + (w^{QG} + \omega)\phi_z) - \omega\Phi_z + w_\phi(\phi_z + \Phi_z) = (M_\phi)_z + S_\phi$$

Table 1. *Run table for the nutrient model experiments*

Run	Figure	MLD	w	β
1	1a	P	I	0
2	1b	P	F	0
3	1c	B	F	0
4	1d	P	F	0.1244
5	1e	B	F	0.1244
6	6a	R	0	0
7	6b	R	F	0
8	6c	R	F	0.1244

The figure in which the horizontal maps of each simulation are displayed is indicated. In these runs the mixed layer depth (MLD) is either persisted (P), balanced (B), or varies in time with realistic forcing (R). The vertical velocity (w) is either zero (0), interior (I), or full (F). The meridional gradient of the Coriolis parameter is either zero (0) or its proper value for this latitude (0.1244).

Here $J(\psi^*,\phi)$ represents the advection of ϕ by the quasigeostrophic streamfunction ψ^* and α is a nondimensional parameter. The wind driven velocity components μ and ν advect both interior and boundary layer quantities. Interior and boundary layer vertical velocities w^{QG} and ω advect material vertically. Passive tracers can be assigned arbitrary sinking velocity w_ϕ. The right hand side of the above equation includes mixing terms $(M_\phi)_z$ and biological forcing functions S_ϕ that represent the transfers between nitrogen constituents.

3. THE NUTRIENT MODEL

In order to examine in detail the physical processes of nutrient flux into the mixed layer, an idealized "nutrient model" was constructed. In this model, nutrients that are transported into the mixed layer are instantaneously exported. In a sense, this model parameterizes an upper ocean biological system that operates at infinite speed. This configuration maintains the maximum possible gradient between the mixed and remnant layers thus providing an upper boundary for the nutrient fluxes caused by transport processes that act on this gradient.

In this set of numerical experiments, various transport mechanisms are examined separately and then combined in a logical manner, building toward the most realistic case in which all of the processes are active. A summary of the simulations described below is shown in Table 1. Transports of three basic types are investigated: (1) those arising from vertical motions due to mesoscale flows and their interaction with the surface layer; (2) those due to β-induced propagation of features; and (3) those due to excursions of the mixed layer primarily caused by atmospheric forcing. First the mixed layer is persisted (held at a constant depth) in order to examine the relative efficacy of transports caused by interior vertical velocities and those generated by wind interactions (runs 1 and 2). Then the partitioning of the upward flux between that which is entrained into the mixed layer and that which is not is quantified by specifying a "balanced" mixed layer situation in which

a constant wind and compensating heat flux cause a constant mixed layer depth in the absence of eddy motions (run 3). In run 4, feature propagation is induced by turning on β with a persisted mixed layer. The relative magnitude of the mesoscale dynamical vertical velocities and the propagation flux is quantified by comparison with run 2. The entrainment partitioning of the propagation flux is examined in run 5, which is the most realistic of the constant forcing experiments in that all eddy related transports are active. Runs 6–8 are used to compare the eddy transports to the nutrient flux due to excursions of the mixed layer caused by realistic atmospheric forcing.

The initial condition used in these experiments is a feature model representation of an isolated eddy characteristic of the Small eddy described in Robinson *et al.* (1993). The use of feature models facilitates the generation of full water column fields from limited data sets by using assumptions about the velocity structure of the features of interest. Estimates of the feature model parameters (eddy radii, swirl speeds and vertical shears) obtained by altimetric and *in situ* observations can therefore be used to analytically compute the streamfunction and vorticity fields required for initialization of the quasigeostrophic model. In the axisymmetric feature model employed here, the velocity increases linearly from the center out to a radius of maximum velocity, beyond which it decays exponentially. There is a linear shear in the vertical down to an assumed level of no motion at 2500 m. This vortex model was chosen to be consistent with both the present data and deeper historical data available in the region.

Horizontal boundary conditions in these and all other simulations discussed in this work are persisted. Each simulation is integrated for 37 days between day 115 and day 152.

3.1. *Run* 1: *persisted MLD*, *interior* w, $\beta = 0$

In the first experiment, the mixed layer is persisted at a constant depth and only the vertical velocity generated by the evolution of the interior is used to advect nitrate across the mixed layer depth interface. Figure 1a shows the alternating upwelling and downwelling regions that develop around the perimeter of the eddy as it evolves. This pattern of vertical velocity rotates cyclonically and is associated with the interior dynamics of the eddy as it develops slight asymmetries during the course of its evolution. The upwelling patches transport nitrate into the mixed layer which results in the export of nitrogen in a ring around the perimeter of the eddy. The width of the band is set by the radial extent of the upwelling patches. There is also noticeable deposition of nitrogen in the center of the eddy that results from a decrease in surface density caused by adjustment of the interior. A time series of the spatially averaged nitrogen export is shown in Fig. 2, curve (a).

3.2. *Run* 2: *persisted MLD*, *full* w, $\beta = 0$

Next the effect of a wind generated surface vertical velocity is examined. The mixed layer is still persisted, but the vertical velocity is now made up of two contributions: one from the eddy interior dynamics described above, and one that arises from the interaction of the wind driven and interior flows. In this run a westerly wind causes Ekman transport toward the south. This flow redistributes the vorticity field through advection of the interior vorticity by the boundary layer velocity. Conservation of potential vorticity requires that the water column stretch (causing upwelling) in areas where vorticity is

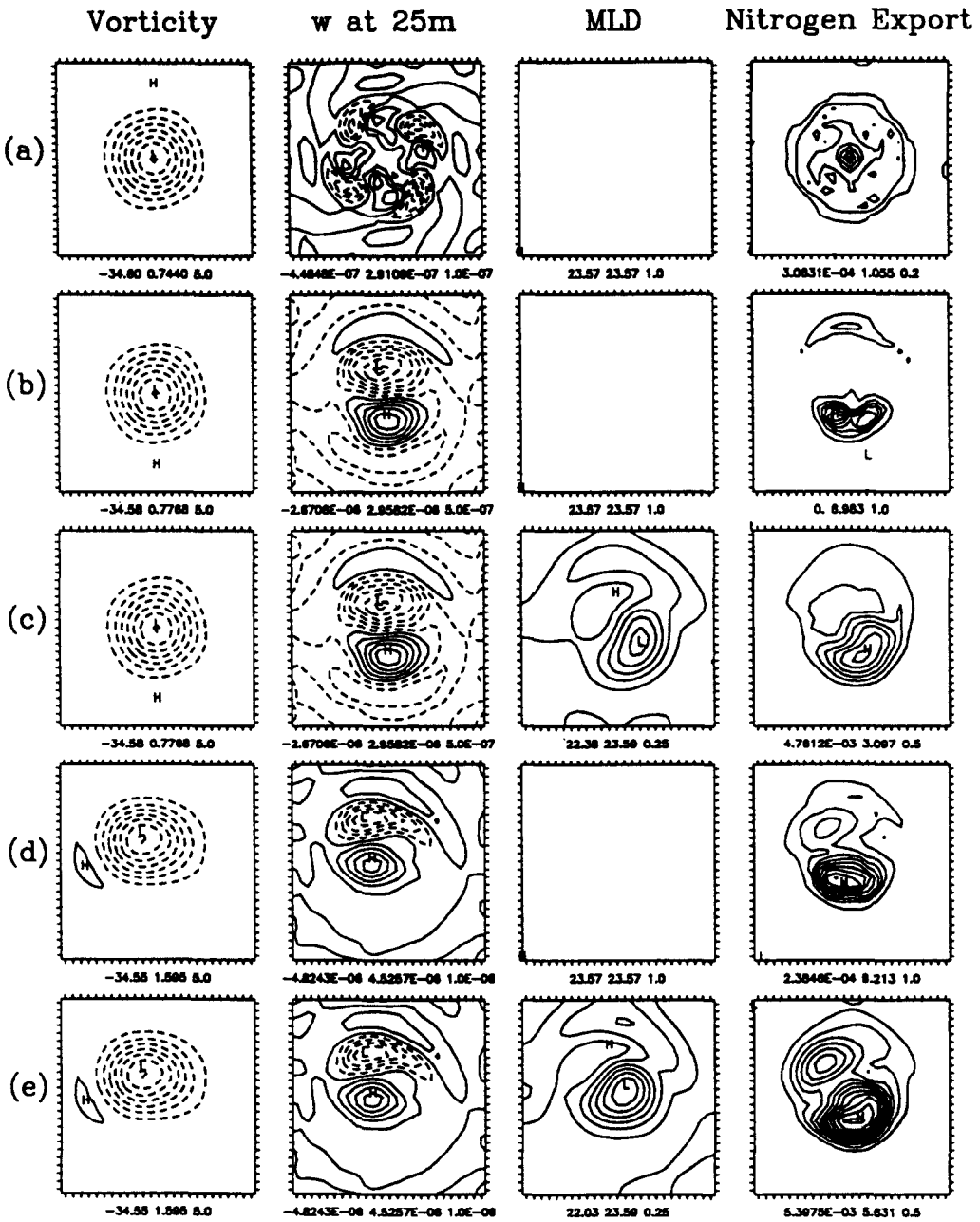

Fig. 1. Maps of vorticity at 50 m (nondimensional), vertical velocity at 25 m (m/s), mixed layer depth (m) and integrated nitrogen export ($[g/cm^2]/8.4 \times 10^{-2}$) after 37 days of integration for runs 1–5 (A–E) listed in Table 1. The locations of the highest and lowest values in each field are denoted by H and L respectively. Positive contours are solid and negative contours are dashed. The minimum, maximum and contour interval are indicated below the map from left to right. These conventions are used in all the following contour maps except where noted.

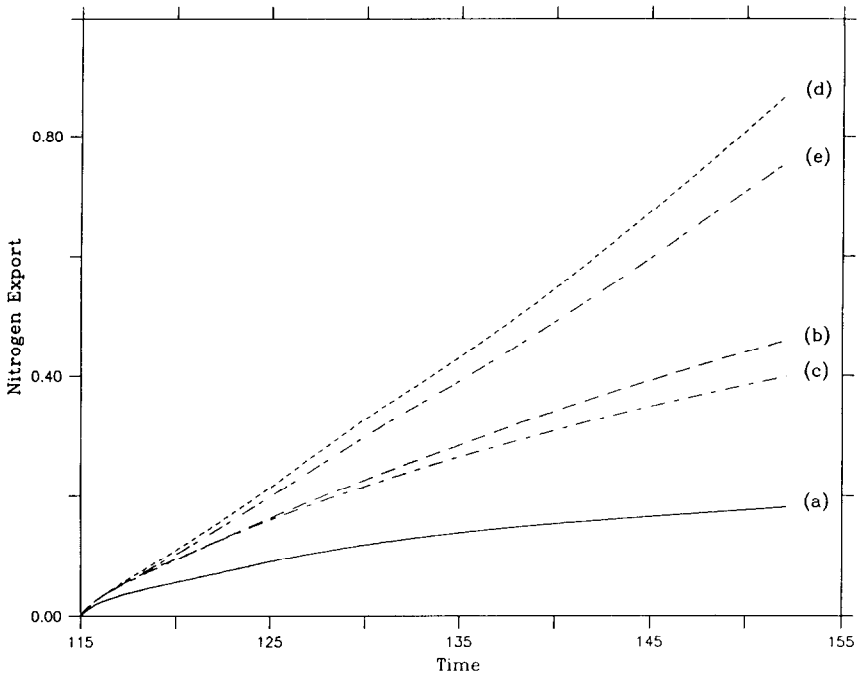

Fig. 2. Spatially averaged nitrogen export ([g/cm^2]/8.4 × 10^{-2}) for the five simulations shown in Fig. 1.

decreasing (the southern flank of the eddy), and compress (causing downwelling) where vorticity is increasing (the northern flank of the eddy). Viewed differently, the advection of the interior velocity by the Ekman velocity causes convergence in the northern part of the eddy and divergence in the southern part. The vertical motions due to this interaction are much larger than those caused by the eddy interior dynamics alone and therefore overshadow the structure of vertical velocity seen in the previous run (Fig. 1b). The more vigorous vertical transport significantly increases the flux of nitrate into the mixed layer, resulting in a much larger accumulation of exported nitrogen (Fig. 2, curve (b)). As expected the region of largest nitrogen export occurs directly underneath the region of upwelling (Fig. 1b).

3.3. *Run* 3: *balanced MLD, full* w, $\beta = 0$

In the next simulation the assumption of a constant mixed layer depth is relaxed. We now use the full mixed layer equation in which there is a three way balance between horizontal advection, vertical advection and entrainment. For comparison with the previous case, the model is forced with the same wind as before, but now positive surface heat flux has been added in order to maintain a finite mixed layer depth. The momentum and heat fluxes balance each other so that the basic state mixed layer is constant. That is, in the absence of any eddy motions the mixed layer depth is uniform and stationary. The surface fluxes were chosen so that the basic state mixed layer resides at the same depth as in

the previous simulations. After 37 days of integration, the mixed layer depth field has stayed approximately constant at the basic state depth over most of the domain except for an area in the southeastern section of the eddy in which it has shoaled (Fig. 1c). The shoaling of the mixed layer in this region is caused by the combination of the upwelling in the southern flank of the eddy pushing the mixed layer toward the surface and the advection of this disturbance by the cyclonic flow of the interior. This behavior reveals a very clear asymmetry in the mixed layer response to vertical motions. In the case of upwelling, there is a partitioning of the upward flux between that which pushes the mixed layer depth upwards and that which is actually entrained into the mixed layer. In the case of downwelling (as occurs in the northern half of the eddy), the vertical velocity causes detrainment of mixed layer fluid. The mixed layer does not descend because the balancing heat and momentum fluxes set the depth of the maximum mixed layer depth, which is coincident with the basic state mixed layer depth. The increase in mixed layer buoyancy with time stratifies the water column, so that the detrained fluid is of lesser buoyancy than the mixed layer, thus preventing deepening of the mixed layer.

The nitrate flux into the mixed layer is decreased with respect to the previous case in which the vertical velocity was used to advect material across an artificially persisted mixed layer depth (Fig. 2, curve (c)). In this simulation, the upward motion pushes the mixed layer toward the surface, and only a portion of the total flux is entrained into the mixed layer. While the bulk of the exported nitrogen accumulates directly below the region of upwelling, there is a significant displacement of the northeastern boundary of the high export region in the direction of the interior flow (Fig. 1c). This results from the entrainment of fluid in the area of shoaled mixed layer depth which has been cyclonically advected by the interior flow. The entrainment occurs where the mixed layer descends toward the basic state depth once it has been advected away from the upwelling region.

It is important to note here that the asymmetry in the mixed layer depth response to vertical motions of opposite sign in this experiment is not common to all types of mixed layer models. For example, simulations carried out with the model of Price *et al.* (1986) show that under similar forcing conditions, the mixed layer depth response is more symmetric. That is, upwelling causes the mixed layer to shoal (as in the present model) and downwelling causes it to deepen (unlike the present model). This symmetry is a result of the different mixing parameterization used in this so called "dynamic instability model" in which mixing is dependent on Richardson number criteria instead of the turbulent kinetic energy budget used in the present model. Therefore the results presented here are to some extent dependent on the particular type of mixed layer model that is being used. However, the primary focus of these experiments is to understand the mechanisms of nutrient injection into the mixed layer (i.e. the upwelling case). In this regime, the response of the two types of mixed layer models is quite similar.

3.4. *Run* 4: *persisted MLD, full* w, $\beta \neq 0$

In all of the previous experiments the parameter β was set to zero so that vertical transport processes could be studied in a stationary eddy. Setting the meridional gradient of the Coriolis parameter to its proper value for this latitude causes the eddy to propagate to the northwest. The pattern of exported nitrogen is similar to the corresponding $\beta = 0$ case (run 2) in that there is accumulation underneath the upwelling region (Fig. 1d). However, in this simulation there is significant export along the northwestern border of the

eddy. Figure 3 shows the instantaneous nitrate flux into the mixed layer on day 151 overlaid on the vorticity field. The transport taking place on the leading edge (with respect to the direction of propagation) of the eddy overshadows the flux caused by the wind driven upwelling. In fact, the integrated nitrogen export on day 151 is approximately twice that of the nonpropagating case (Fig. 2, curve (d)).

This is a simple transport mechanism that can be interpreted as the "propagation flux". Consider the propagating disturbance schematized in Fig. 4. At time t_1 a given nutrient surface is domed upward in a cyclonic vortex so that it penetrates the mixed layer. Biological processes remove this excess nitrate and if the eddy remains at rest there will be no further nutrient supply. This is not necessarily the case when the feature is moving. If the propagation is purely linear, a point (a) at time t_1 will rise to point (c) at time t_2 resulting in an injection of nutrient along the leading edge of the disturbance. If the propagation is purely nonlinear and the vortex moves along as a coherent structure, a point (a) at time t_1 will simply translate to point (b) at time t_2; in this case there is no flux into the mixed layer. The efficacy of this mechanism therefore lies in the level of nonlinearity in the oceanic flow of interest. In the linear case, analytic estimation of the flux is straightforward. The slope of the nitrate surfaces at the base of the mixed layer is approximately 1 part in 500 (Fig. 5). Multiplying this slope by the observed propagation speed of 1.5 km per day gives an effective vertical velocity of 3 m per day. The flux is simply the product of the vertical velocity and the nitrate gradient at the base of the mixed layer. The maximum instantaneous nitrate flux in the simulation (Fig. 4) is nearly identical to this flux estimate, indicating the propagation of the vortex is mostly linear.

3.5. *Run* 5: *balanced MLD*, *full* w, $\beta \neq 0$

In this most realistic of all of the constant forcing experiments all of the previously mentioned transport mechanisms are active in the balanced mixed layer configuration. The resulting nitrogen export (Fig. 1e) is made up of patterns observed in the preceding runs. The integrated export (Fig. 2, curve (e)) is somewhat less than in run 4 because of the partitioning of the upward flux. This causes a relative decrease in the export due to wind driven upwelling, accentuating the propagation flux on the leading edge of the vortex.

3.6. *Run* 6: *realistic forcing*, $w = 0, \beta = 0$

In the remaining three runs the model is forced with time varying atmospheric fluxes derived from shipboard meteorological observations. In the first case (run 6) both the vertical velocity and β are artificially set to zero in order to provide a benchmark for the flux that results from large scale excursions of the mixed layer. The pattern of exported nitrogen (Fig. 6a) is an image of the initial nitrate distribution as the mixed layer has captured material from the uplifted density surfaces inside the vortex in its numerous descents into the remnant layer. The time series of nitrogen export (Fig. 7, curve (a)) reveals that the largest flux of nitrate occurs right in the beginning of the simulation as the mixed layer deepens from its initial depth of 23 m to nearly 60 m. The next largest flux happens just a few days later as the mixed layer reaches its deepest point of the simulation, just below 60 m. Because the nutrient model removes all of the nitrate from this depth interval at this time, subsequent nutrient fluxes are much smaller. In fact, the only avenue for further nutrient capture is for the mixed layer to shoal, allowing nitrate to diffuse

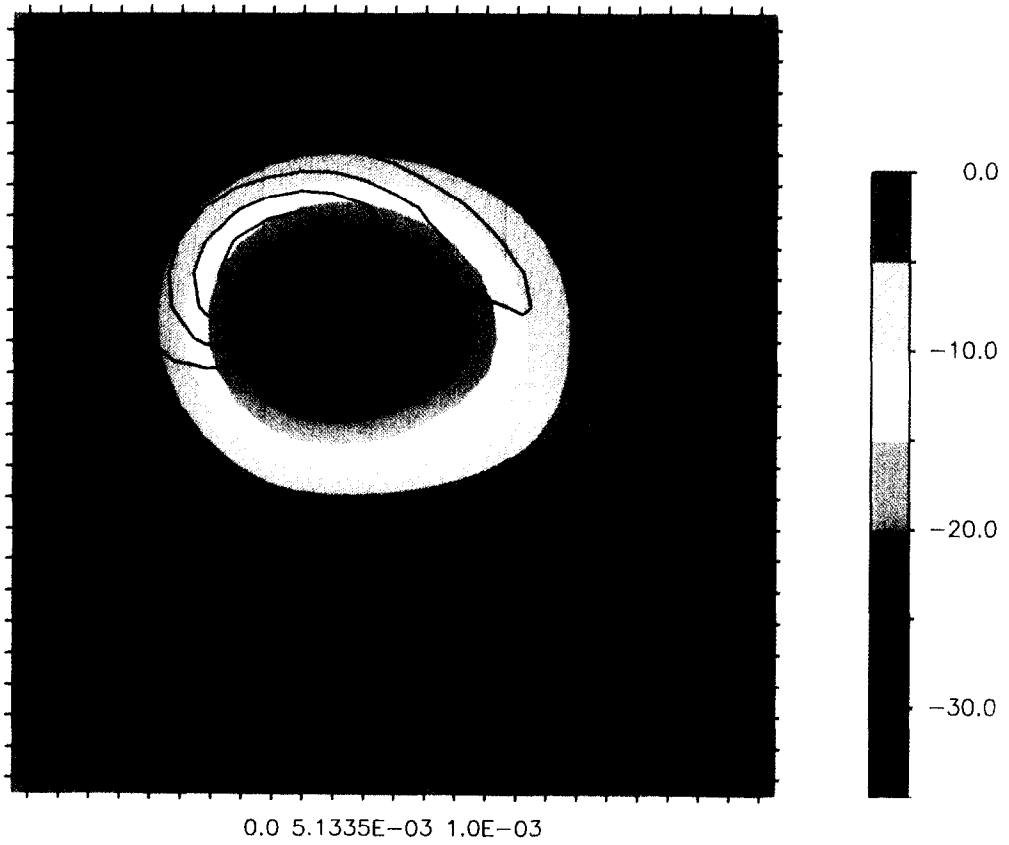

Fig. 3. Instantaneous nitrate flux into the mixed layer (units of 5.3 g/m^2/d) contoured over the 50 m vorticity field. The color bar shows the shading of the vorticity field in nondimensional units.

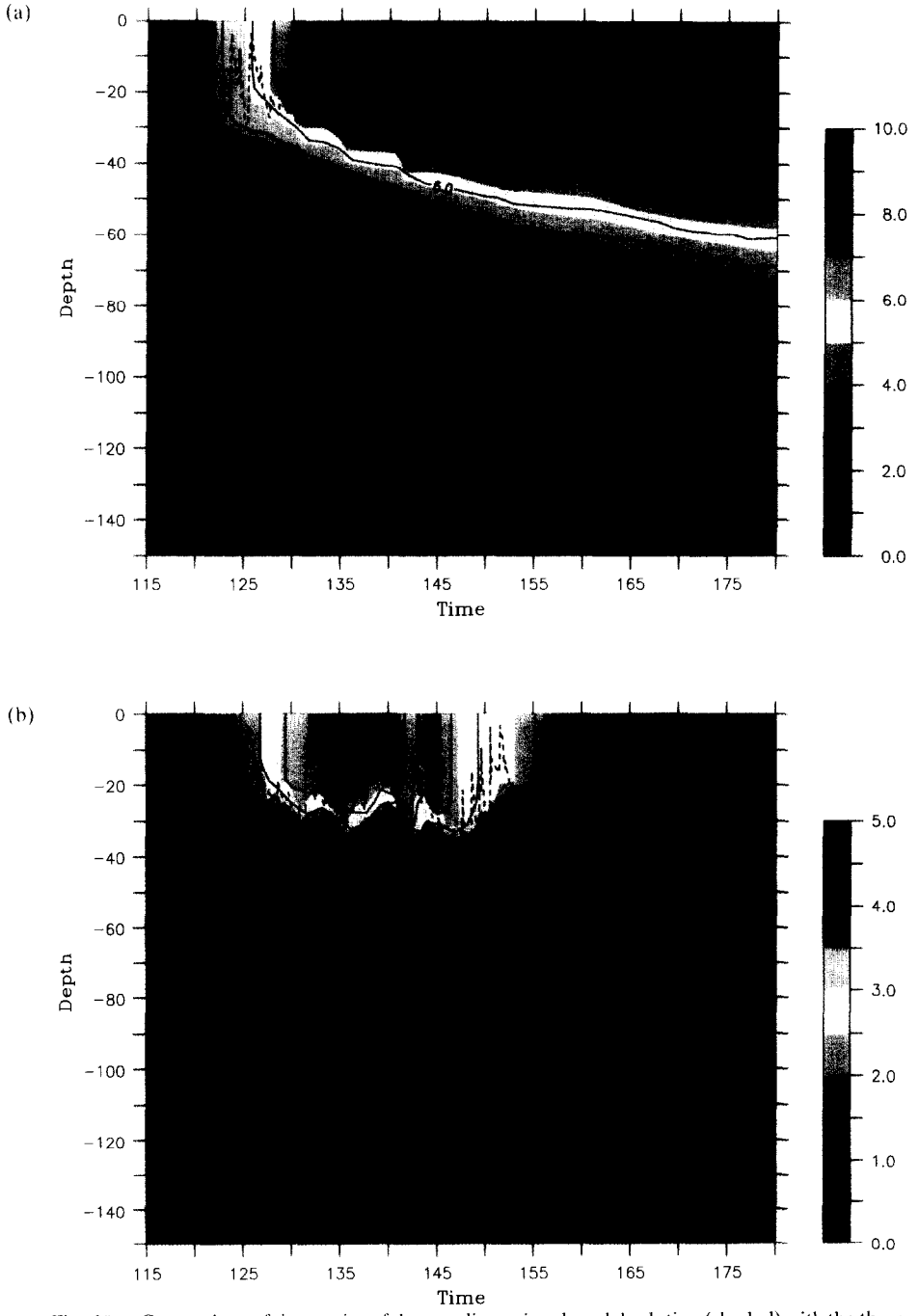

Fig. 18. Comparison of time series of the one dimensional model solution (shaded) with the three dimensional model solution (overlaid contours) inside the Small eddy: (a) nitrate, (b) phytoplankton, (c) heterotrophs and (d) ammonium. The one dimensional simulation shows more structure in time as the temporal resolution of the one dimensional record is 0.5 days, while that of the three dimensional record is 1.5 days. The dashed line shows the mixed layer depth.

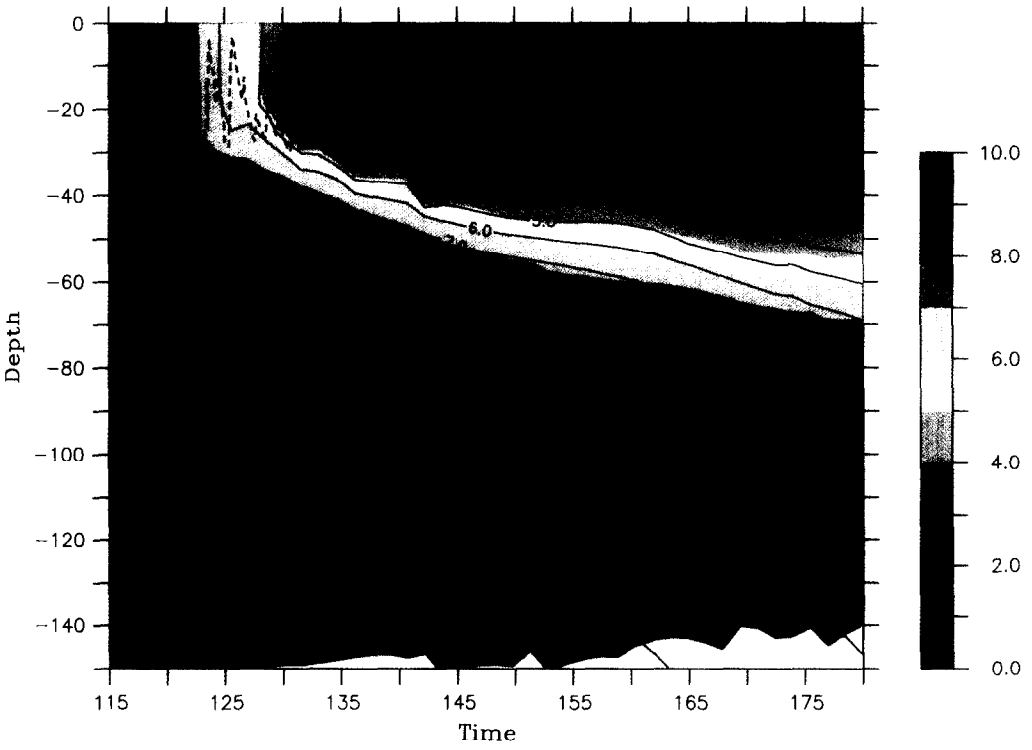

Fig. 25. Comparison of time series of the mixed layer nitrate concentration inside the Small eddy in the isolated case (shaded) and the three eddy case (overlaid contours). The dashed line shows the mixed layer depth.

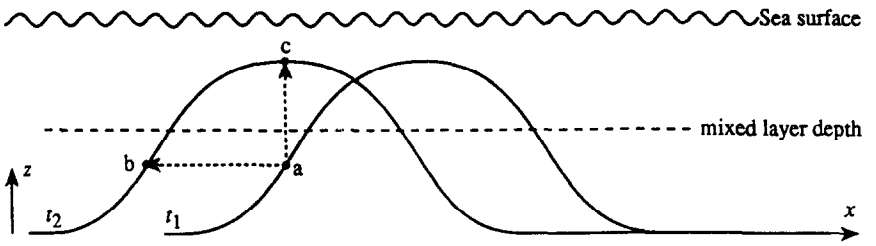

Fig. 4. A schematic representation of the propagation flux mechanism, showing an uplifted nitrate surface in a cyclonic vortex at times t_1 and t_2.

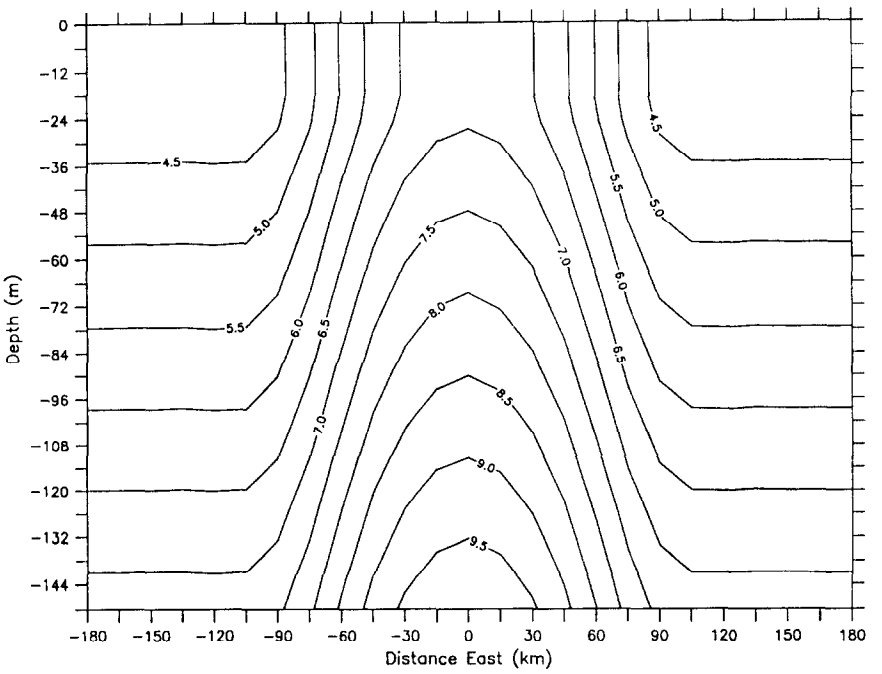

Fig. 5. A vertical section of the initial nitrate distribution across the Small eddy (μM).

upward in the remnant layer. Only then can the mixed layer scavenge additional nutrient from the remnant layer as it deepens.

This behavior demonstrates how the nutrient model exaggerates the nitrate flux in the realistic forcing experiments much more than in the constant forcing cases. Rapid deepening of the mixed layer in convective or wind driven events does create effective vertical velocities much larger than those generated by eddy effects, causing substantial flux into the mixed layer. However, these deepening events are followed by shoaling events in which large detrainment fluxes occur. In the nutrient model, the flux of nitrate from the mixed layer to the remnant layer is identically zero as the mixed layer shoals because nitrate is *instantaneously* removed from the mixed layer. This is of course not the case in the real ocean because biological removal processes take time. When the mixed

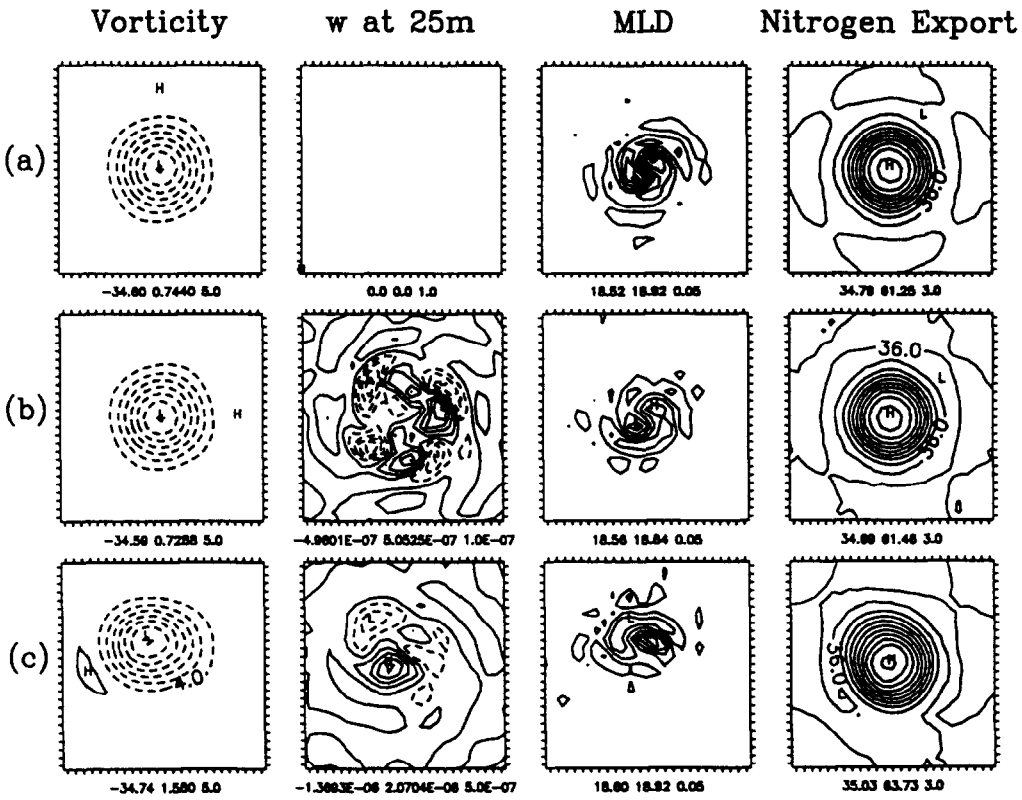

Fig. 6. Vorticity at 50 m (nondimensional), vertical velocity at 25 m (m/s), mixed layer depth (m) and integrated nitrogen export ([g/cm^2]/8.4 × 10^{-2}) on day 152 for runs 6–8 (a–c) listed in Table 1.

layer shoals after a deepening event, the unused nitrate is detrained and remains available for entrainment during subsequent deepening events. This process is not represented in the nutrient model.

3.7. *Run* 7: *realistic forcing*, $w \neq 0, \beta = 0$

Activating the full vertical velocity changes the overall solution very little, as the problem is dominated by the one dimensional transport processes. Figure 6b shows that the pattern of nitrogen export is nearly identical to the previous case. The amount of export is only slightly enhanced by the wind driven and eddy induced upwelling; the integrated export curve in Fig. 7, curve (b), is almost coincident with that of run 6.

3.8. *Run* 8: *realistic forcing*, $w \neq 0, \beta \neq 0$

Allowing the vortex to propagate also makes little difference in the solution (Fig. 6c). The propagation flux makes the integrated export distinguishably larger than the previous two cases, but the difference is quite small (Fig. 7, curve (c)).

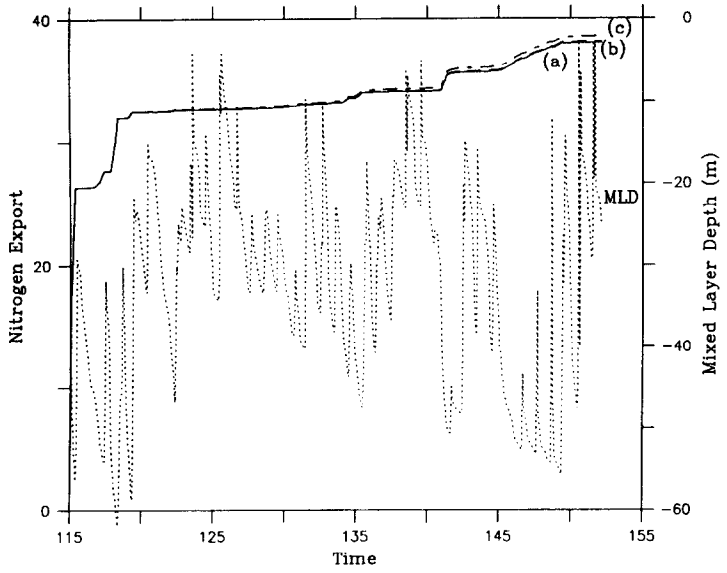

Fig. 7. Spatially averaged nitrogen export ([g/cm^2]/8.4 × 10^{-2}) for the three simulations shown in Fig. 6. Run 6 (curve a) is the solid line, run 7 (curve b) is a dashed line that is nearly coincident with (a), and run 8 (curve c) is the variable dashed line. The mixed layer depth is shown as a dotted line.

4. THREE DIMENSIONAL BLOOM SIMULATION: FORCING

Having examined nutrient flux processes in idealized numerical experiments, we now move on to more realistic simulations using the full interdisciplinary model. The physical model is forced with the observed winds and heat fluxes inferred from shipboard meteorological measurements during the time period in which they are available. It is of interest here to carry the simulations out further in time as the eddy effects become more pronounced after the transition to oligotrophy which takes place at the very end of the data set. For this purpose meteorological quantities for the region are extracted from the twice daily output from the European Center for Medium Range Weather Forecasting (ECMWF) atmospheric general circulation model. To verify the accuracy of the ECMWF fields for this region, model output was compared to the shipboard measurements for the period between days 115–151 (Fig. 8). Note that the temporal coverage of the shipboard records has been expanded beyond that reported in Robinson *et al.* (1993) with the recovery of additional data originally thought to have been lost. The wind speed records (Fig. 8a) agree extremely well except for three periods on or around days 121, 124 and 134 in which the ECMWF wind is significantly stronger than that observed. The wind direction is also represented quite well by the ECMWF model (Fig. 8b). Of course the observations show much more variability than the GCM can resolve, but the main features of the record are well reproduced. The surface heat flux inferred from the ECMWF fields also compares well (Fig. 8c). Except for during the storm on day 142 the heat fluxes computed from the two sources are quite similar. These heat flux calculations depend very much on the air–sea temperature gradient. During the period in which the ships were at sea, observed sea surface temperature is used in the heat flux computation. Beyond day 151 no sea surface temperature measurements are available so the model temperature is used.

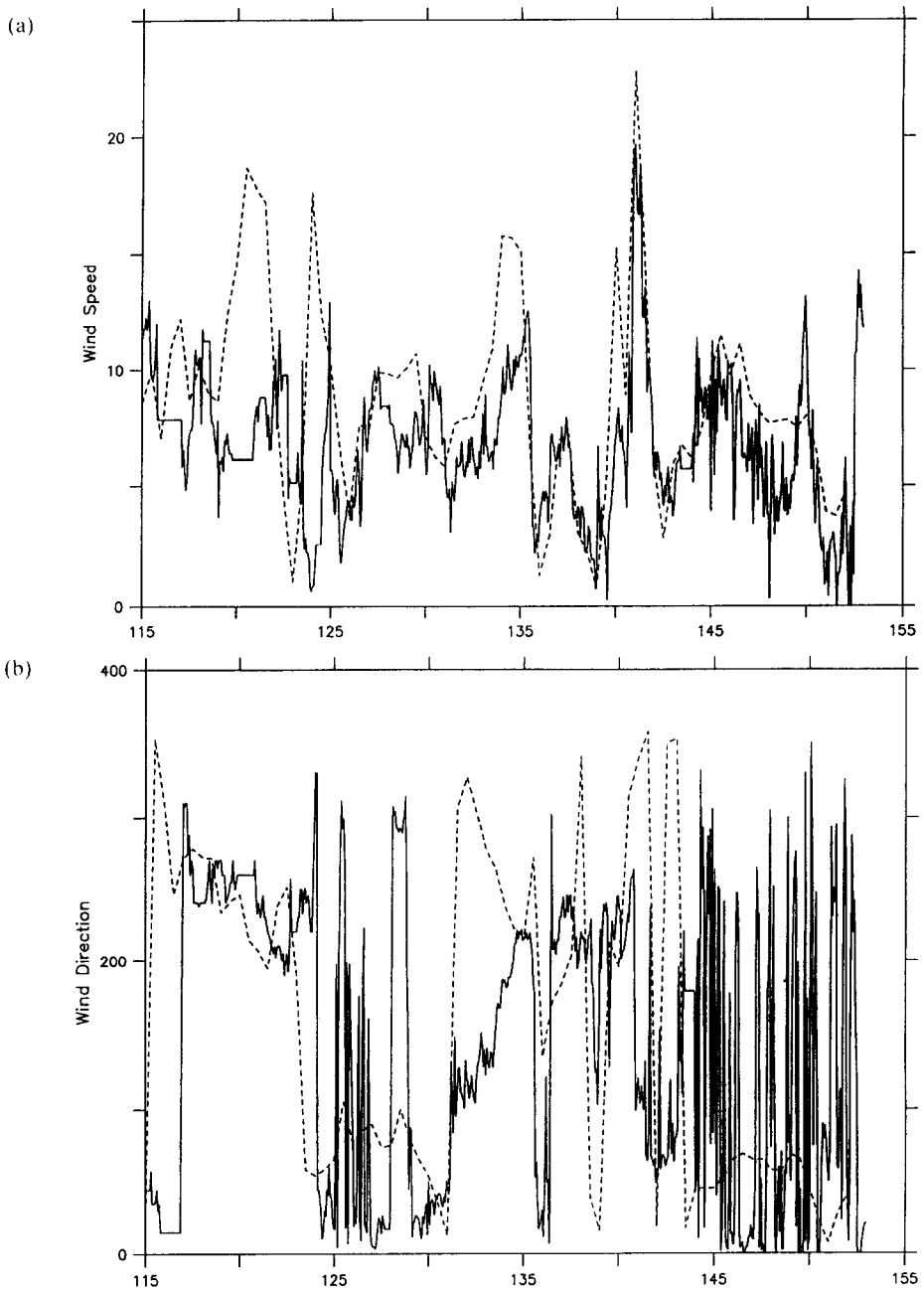

Fig. 8.

The flux of shortwave solar radiation is also needed for the later period for which there is no data. The radiation incident on the sea surface for a clear sky is directly calculable using standard algorithms (List, 1951). Because no observations of cloud cover are available after the ships left the area, their attenuation of the short wave flux must be estimated.

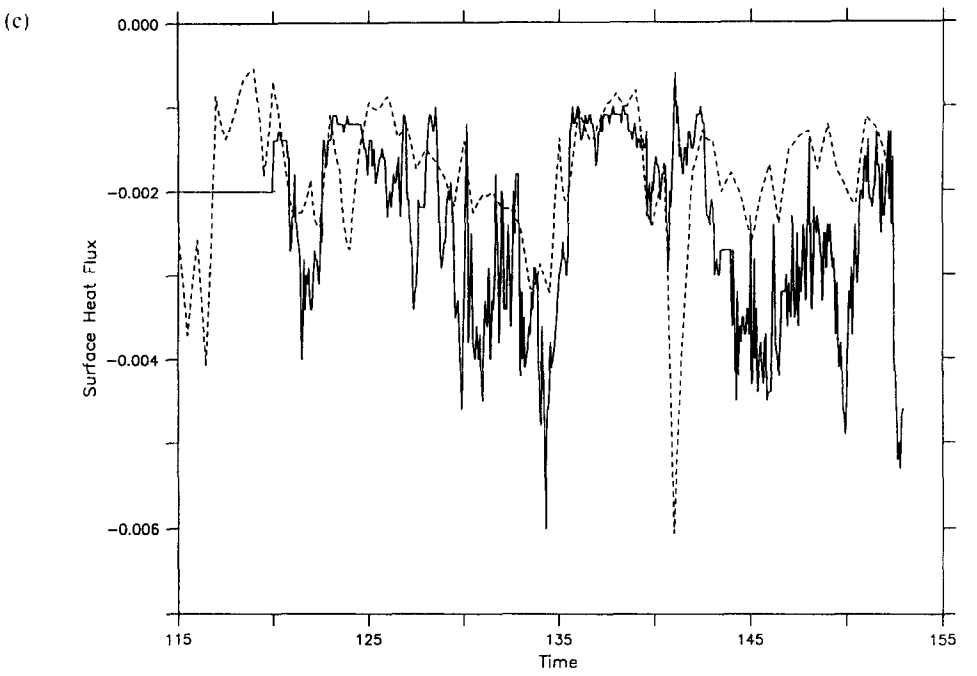

Fig. 8. Comparison of observations (solid line) with twice daily predictions from the ECMWF model (dashed line) for (a) wind speed (m/s) and (b) wind direction (degrees true). Panel (c) shows a comparison of the surface heat flux (cal/cm^2) estimated from shipboard meteorological observations (solid line) with those estimated from twice daily predictions of atmospheric conditions from the ECMWF model and sea surface temperature from the coupled quasigeostrophic and surface boundary layer model (dashed line). The heat flux estimated from the shipboard measurements is constant for the first five days because of missing values.

Historical data on cloud cover for the region indicate that cloud cover changes little over the two month period between days 115–180 (Miller, 1971). It is therefore reasonable to use the same effective cloud cover for days 151–180 as was present during days 115–151. To estimate the effective attenuation a simple ratio between the mean observed irradiance at the sea surface and the clear sky model prediction is computed for the period.

The combined records of observed and computed fluxes used to force the model in these simulations is shown in Fig. 9.

5. THREE DIMENSIONAL BLOOM SIMULATION: THE SMALL EDDY

In this experiment the bloom is simulated in a 360 km^2 domain with the Small eddy in isolation. The central biological parameter set described in the one dimensional model tuning experiments in MMR95 is used. The model is initialized on Day 115 with an axisymmetric feature model representation of the Small eddy (Fig. 10). The surface geostrophic velocity in the eddy increases linearly to 25 cm/s at a radius of 70 km beyond which it decays exponentially. There is linear shear in the vertical down to a level of no motion at 2500 m. The vorticity distribution shown in Fig. 10 consists of contributions from both the relative and thermal vorticity of the eddy. In this situation the thermal vorticity

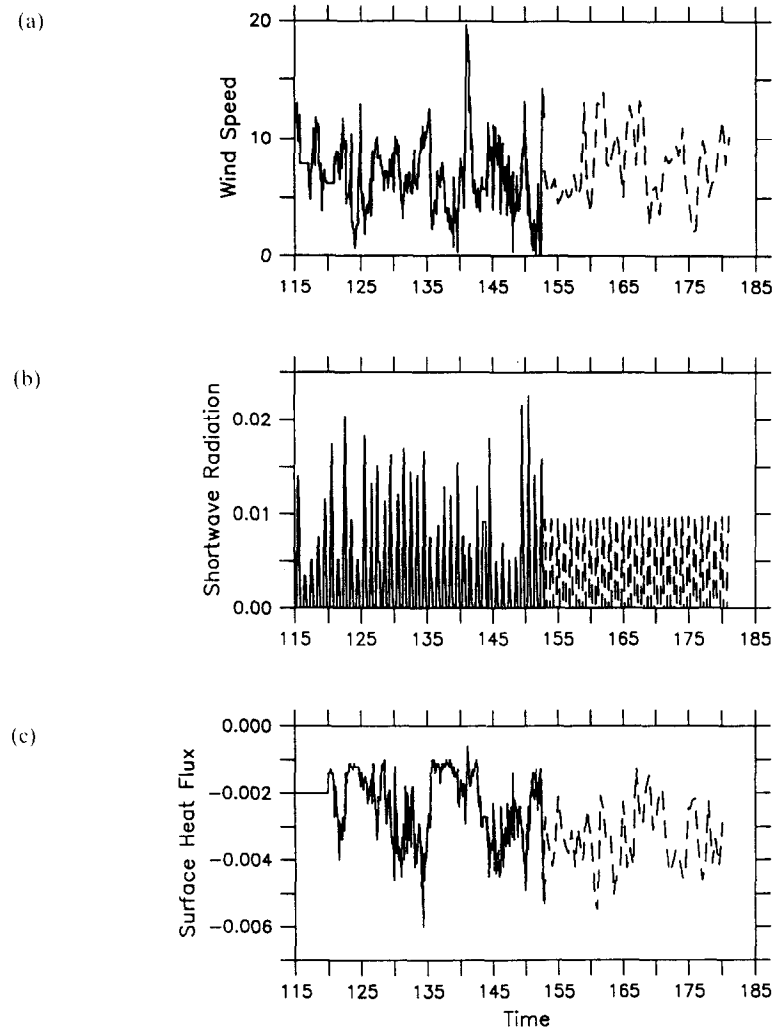

Fig. 9. Time series of surface fluxes used to force the physical model: (a) wind speed (m/s), (b) shortwave radiation (cal/cm^2) and (c) surface heat flux (cal/cm^2). Solid lines are used where shipboard meteorological observations are available and dashed lines are used where the quantities are estimated from model output (see text).

signal overshadows the relative vorticity so that the total vorticity inside this cyclonic feature is negative. This initialization is a result of careful tuning of the model to the available data and thus represents an improvement to the initial conditions used in Robinson *et al.* (1993) in which the sign of the vorticity perturbations caused by the three eddies was positive. The vertical velocity is identically zero in the initial condition, and the top density pattern mimics the vorticity distribution. The biological model initial conditions (Fig. 11) consist of constant values for phytoplankton, heterotrophs and ammonium. Nitrate is initialized from the observed nitrate versus sigma–*t* relationship. See MMR95 for a more detailed description of the biological initial conditions.

After 36 days of integration (Day 151), the eddy has propagated approximately 54 km to

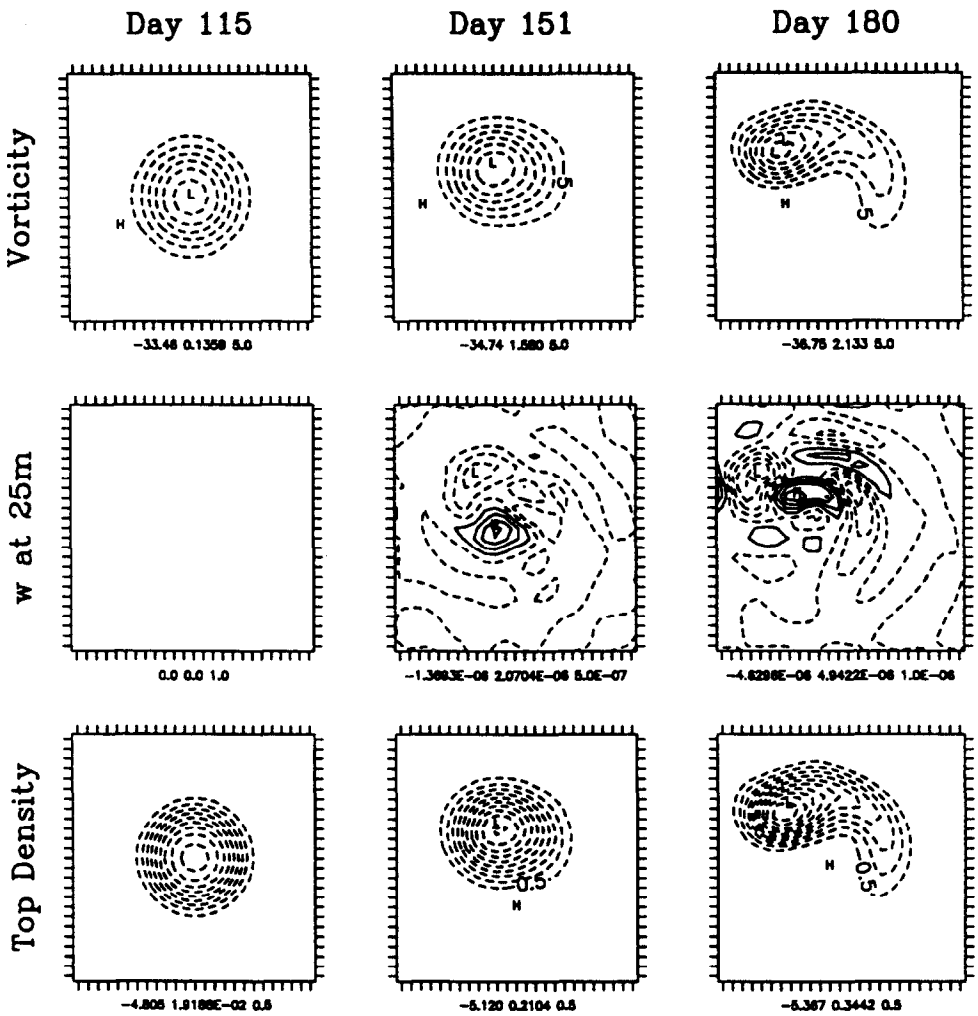

Fig. 10. Maps of vorticity at 50 m (nondimensional), vertical velocity at 25 m (m/s) and top density $\Gamma^2 \sigma \psi_z|_{z=0}$ (nondimensional) in the initial condition (day 115) and after 36 and 65 days of integration.

the north–northwest and has become noticeably asymmetric. This behavior is characteristic of that observed in other numerical simulations of isolated vortices (e.g. McWilliams and Flierl, 1979). Submesoscale patches of vertical velocity have developed as a result of both the internal dynamics of the eddy and the interaction with the wind driven surface current. The evolution of the top density field is quite similar to that of the vorticity, and the maximum perturbation has increased by approximately 7%.

By Day 151, most of the nitrate has been removed from the mixed layer (Fig. 11) in a pronounced bloom event. Phytoplankton and heterotrophic biomass distributions reflect the pattern of the initial nitrate field, as the increased availability of nitrate inside the eddy has allowed the bloom to proceed much further in its interior. Mixed layer ammonium concentrations are quite low due to phytoplankton uptake, but show the same pattern of

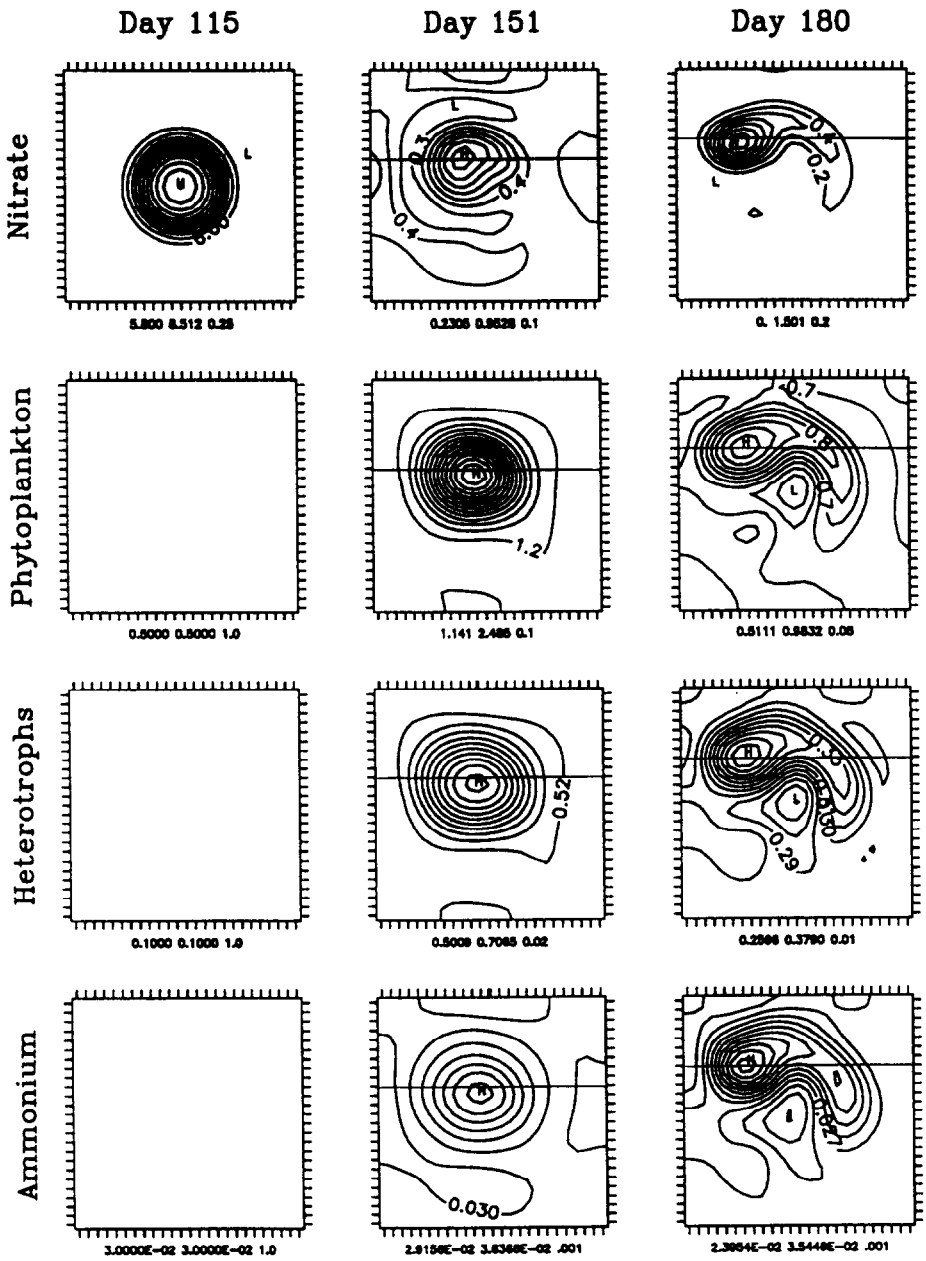

Fig. 11. Maps of mixed layer nitrate, phytoplankton, heterotrophs and ammonium (μM) in the initial condition (day 115) and after 36 and 65 days of integration.

enhancement inside the eddy because more nitrogen is being cycled through the phytoplankton–heterotroph–ammonium loop due to the initially higher nitrate concentration.

Vertical sections of the model solutions on day 151 from west to east along the line

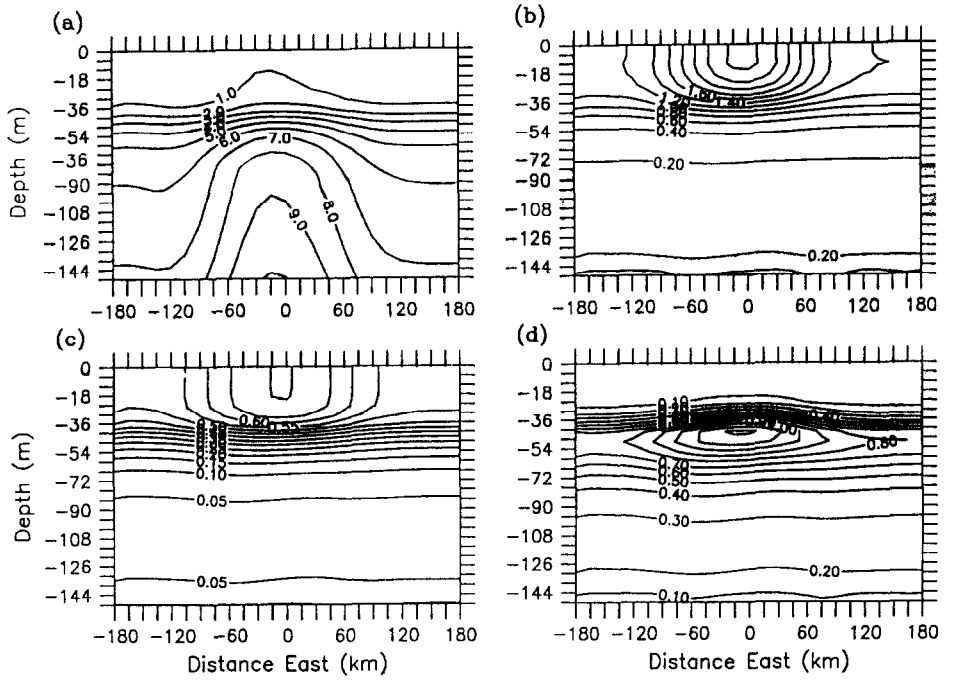

Fig. 12. Vertical sections of (a) nitrate, (b) phytoplankton, (c) heterotrophs and (d) ammonium (μM) taken from west to east across the Small eddy along the line indicated in Fig. 11 on day 151.

indicated in Fig. 11 are shown in Fig. 12. The removal of nitrate from the near surface region has produced a strong nitracline centered at approximately 45 m (Fig. 12a). The nitracline is slightly shallower in the eddy interior, where the doming of the nitrate surfaces is still quite evident in the deeper layers. Phytoplankton (Fig. 12b) and heterotrophic (Fig. 12c) biomass sections show enhancement in the eddy interior in the surface layers with strong gradients in approximately the same location as the nitracline. The gradients have a pattern opposite to the nitracline in that they are slightly deeper in the interior of the eddy. The ammonium distribution (Fig. 12d) has a pronounced subsurface maximum at around 45 m which is consistent with observations (MMR95). The subsurface maximum is significantly enhanced by the increased recycling inside the eddy. Vertical sections of some biological diagnostic quantities are shown in Fig. 13. Primary production (Fig. 13a) is enhanced in the surface layers inside the eddy mostly because of the increased biomass. At depth the surfaces of constant primary production are domed because self shading by the enhanced phytoplankton biomass has noticeably altered the light field (Fig. 13d). There is a sharp vertical gradient in the f-ratio at around 25 m where significant concentrations of ammonium exist (Fig. 13b). The highest f-ratio values are in the interior of the eddy where the enhancement of nitrate overshadows that of ammonium. The nutrient limitation factor Q in the phytoplankton growth equation is shown in Fig. 13c. See MMR95 for more details concerning Q; phytoplankton growth is limited by nutrients as Q approaches 0 and unlimited by nutrients as Q approaches 1. Figure 13c reveals that on day 151 sufficient concentrations of nutrient remain to preclude any strong nutrient limitation, even in the mixed layer. The nutricline is located at the shallowest depth at which either nutrient is

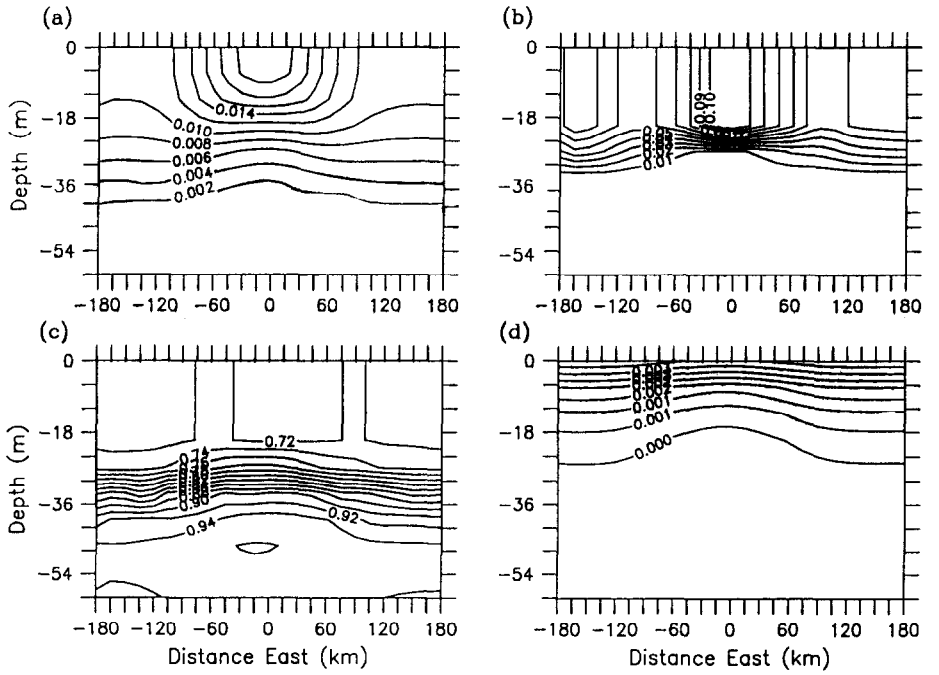

Fig. 13. Vertical sections of (a) primary production ($gNO_3/m^2/day$), (b) *f*-ratio (nondimensional), (c) nutrient limitation factor Q (nondimensional) and (d) photosynthetically available radiation ($cal/cm^2/s$) from west to east across the Small eddy along the line indicated in Fig. 11 on day 151.

available in a concentration sufficient to allow phytoplankton uptake. This occurs at the ammonium gradient (30 m), which is much shallower than the nitracline (45 m). The enhanced surface nutrient concentrations inside the eddy slightly increase Q in that region.

Between days 151 and 180 the core of the vorticity depression propagates at approximately the same speed but in a more westerly direction (Fig. 10). The asymmetry of the vorticity distribution has become much more exaggerated, as the eddy has evolved into an ellipsoid with a long vortex "tail" on its eastern flank. The vertical velocity has increased by a factor of 2–3, with patches of upwelling in the northern and southern portions of the eddy, and downwelling to the east and west. The top density perturbation has continued to deepen and its pattern reflects the distortion of the vorticity field.

By day 180 nearly all of the nitrate has been removed from the mixed layer in the waters surrounding the small eddy, reflecting a post-bloom situation (Fig. 11). More than half of the phytoplankton biomass produced during the bloom has been consumed by heterotrophs. Inside the eddy the situation is quite different. The mixed layer nitrate concentration has actually *increased* to values in excess of (1 μM) in the central core. Nitrate enhancement is evident from the eddy core out to the vortex tail. The increased nitrate supply has sustained post-bloom phytoplankton growth, but heterotrophic consumption limits phytoplankton accumulation. The phytoplankton, heterotroph and ammonium distribution patterns are quite similar to that of nitrate, except for an area of significantly lower concentration just to the south of the vortex tail. Close examination of a time series of the nitrate and phytoplankton fields (Fig. 14) reveals the origin of this feature. On day 160 the central core of high nitrate in the small eddy has an area of low concentration

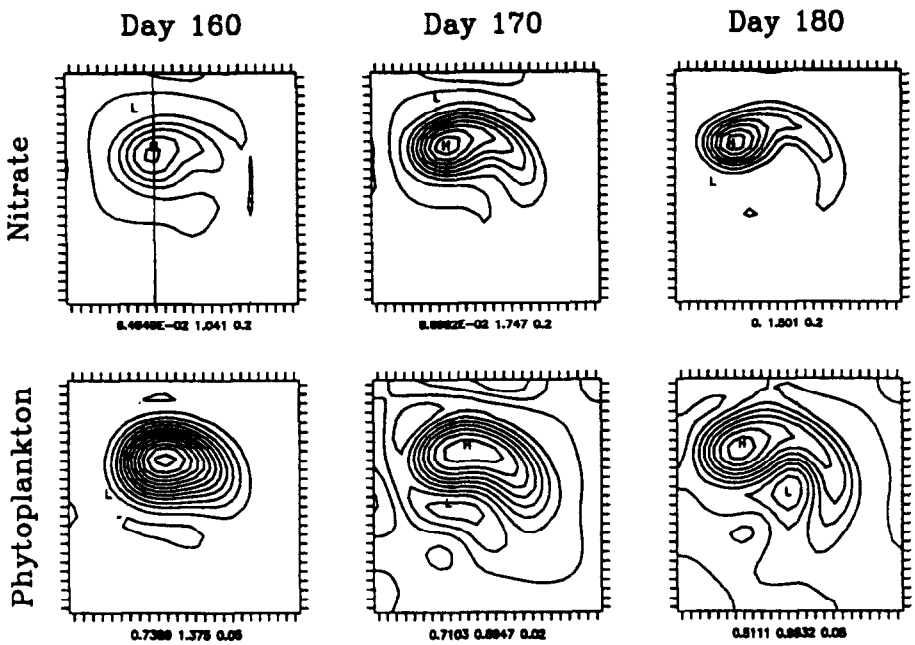

Fig. 14. A time series of mixed layer nitrate and phytoplankton fields from day 160 to 180.

surrounding it. A vertical section of nitrate on this day shows that the nutrient surfaces dip downward slightly on the borders of the eddy and then rise again to the background level (Fig. 15). This structure can be interpreted as the disturbance caused by wave radiation as the vortex decays. The low nutrient band around the eddy results in the development of phytoplankton biomass minima in this region by day 160 (Fig. 14). By day 170, the biomass minimum to the south of the eddy has become more pronounced while the anomaly in other quadrants surrounding the eddy is masked by the propagation of the vortex. The strong minimum to the south of the eddy on day 170 is subsequently advected eastward during the vortex tail formation and by day 180 it is tucked tightly against the southern flank of the eddy as the tail begins to wrap around it.

Vertical sections of the model solutions on day 180 from west to east along the line indicated in Fig. 11 are shown in Fig. 16. Outside the eddy the nitracline has deepened due to removal by phytoplankton and broadened somewhat via diffusive processes (Fig. 16a). In the interior of the eddy the nitracline is closer to the surface and the outcropping of the (1 μM) isocline of nitrate is evident. At depth the doming of the nutrient surfaces has spread eastward with the formation of the vortex tail. The phytoplankton, heterotroph and ammonium (Fig. 16b–d) distributions are similar in pattern to those on day 151 with the exception that the eddy anomalies extend further to the east in the vortex tail. In general the concentrations of the material are lower because of consumption and export. The subsurface ammonium maximum has descended due to heterotrophic grazing on sinking phytoplankton. Biological diagnostic quantities along the same section are shown in Fig. 17. The rate of primary production (Fig. 17a) has decreased considerably with the reduction in phytoplankton biomass. The f-ratio (Fig. 17b) has risen in the interior of the

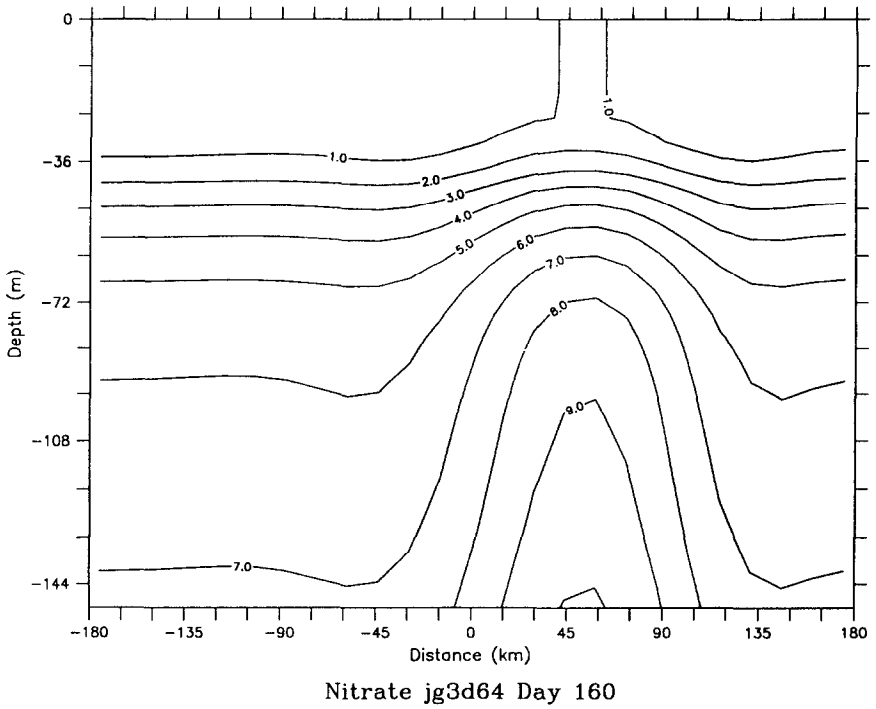

Fig. 15. A vertical section of nitrate from south to north across the Small eddy along the line indicated in Fig. 14 on day 160.

eddy due to the greater availability of nitrate. Areas of nutrient depletion on the borders of the eddy are visible as minima in the nutrient limitation factor Q (Fig. 17c). Ammonium concentrations in these regions are slightly higher than nitrate (taking the ammonium preference into account) so the f-ratio is lower in these areas. The mesoscale signal in the light field is smaller in magnitude as compared to day 151 as the lower phytoplankton biomass reduces self shading (Fig. 17d).

Comparison of the three dimensional model solutions with the one dimensional results is facilitated by extracting a time series of profiles from the three dimensional fields. Far from the eddy, the three dimensional results are nearly identical to the one dimensional solutions and therefore are not shown here. Inside the eddy there are noticeable differences (Fig. 18). At depth the nitrate contours of the three dimensional solution rise in time while those in the one dimensional case do not, indicating that upwelling is occurring in the interior of the eddy (Fig. 18a). This supply of nutrient effectively slows the descent of the nitrate surfaces in the euphotic zone in the three dimensional simulation. Thus the upwelled flux serves to partially offset the nutrient removal by phytoplankton so that nitrate concentrations are generally higher in the three dimensional case. A striking aspect of this behavior is that the increase in available nutrient results in little additional phytoplankton biomass accumulation as compared with the one dimensional simulation inside the eddy (Fig. 18b). This is a result of the tight coupling between the phytoplankton and heterotrophic populations, which is quite evident in the time series of the integrated nitrogen reservoirs (Fig. 19). During the phytoplankton bloom there is a corresponding

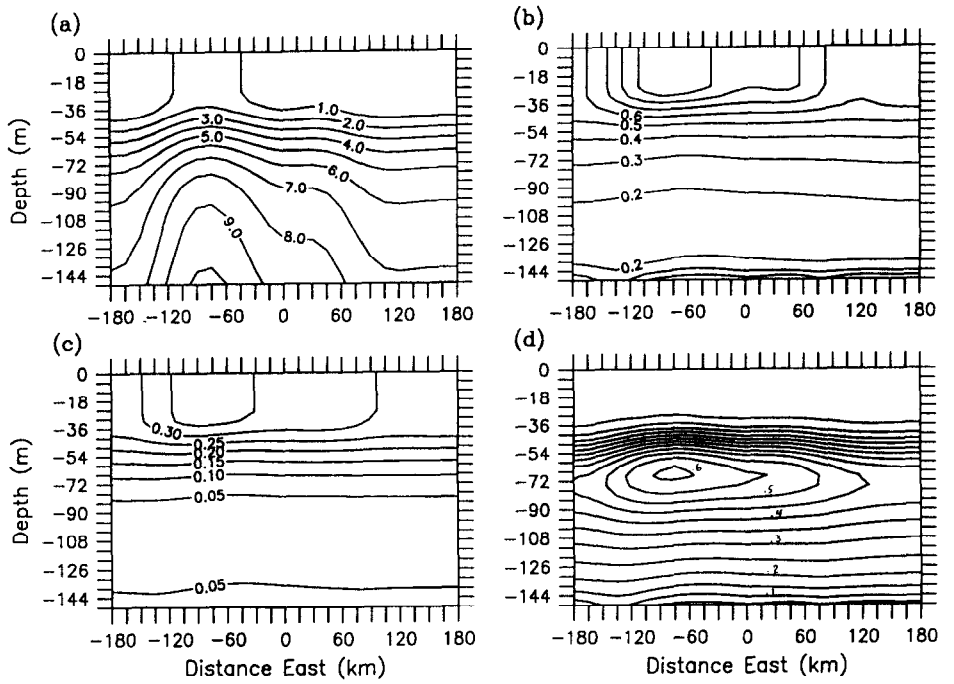

Fig. 16. Vertical sections of (a) nitrate, (b) phytoplankton, (c) heterotrophs and (d) ammonium (μM) taken from west to east across the Small eddy along the line indicated in Fig. 11 on day 180.

increase in heterotrophic biomass that lags by only a few days. As soon as the phytoplankton become nutrient stressed, the heterotrophs overtake them and phytoplankton biomass begins to decline. Heterotrophic biomass also declines as the bulk of the material fixed during the bloom is exported to depth. Even subsequent to the bloom most of the nitrate that is removed is exported on a fairly short time scale; that is, late in the simulation (days 165–180) the rate of nitrate removal and the rate of nitrogen export are roughly equivalent, resulting in fairly stable biomass distribution.

Figure 20 compares time series of mixed layer nitrate for the one dimensional and three dimensional simulations inside and outside the small eddy. During the first part of the simulation the one dimensional and three dimensional solutions in the two locations are quite similar, as the main signal is a one dimensional bloom process in which the evolution is, to a large extent, determined by the initial nitrate distribution. Because the initial condition is mixed beyond the euphotic zone, no significant gradients exist in the region in which physical transports can effectively supply nutrient to the surface layers. However, during the bloom phytoplankton uptake creates a sharp nitracline on which physical transport processes operate. After about day 145 three dimensional mesoscale transport processes significantly enhance the mixed layer nitrate concentration inside the small eddy. Toward the end of the simulation the concentration predicted by the three dimensional model is more than twice that of the one dimensional case. This enhancement is attributable to a combination of the propagation flux mechanism discussed in section 3 and the lifting of the nitrate surfaces in the interior of the eddy due to the dynamics of the vortex evolution.

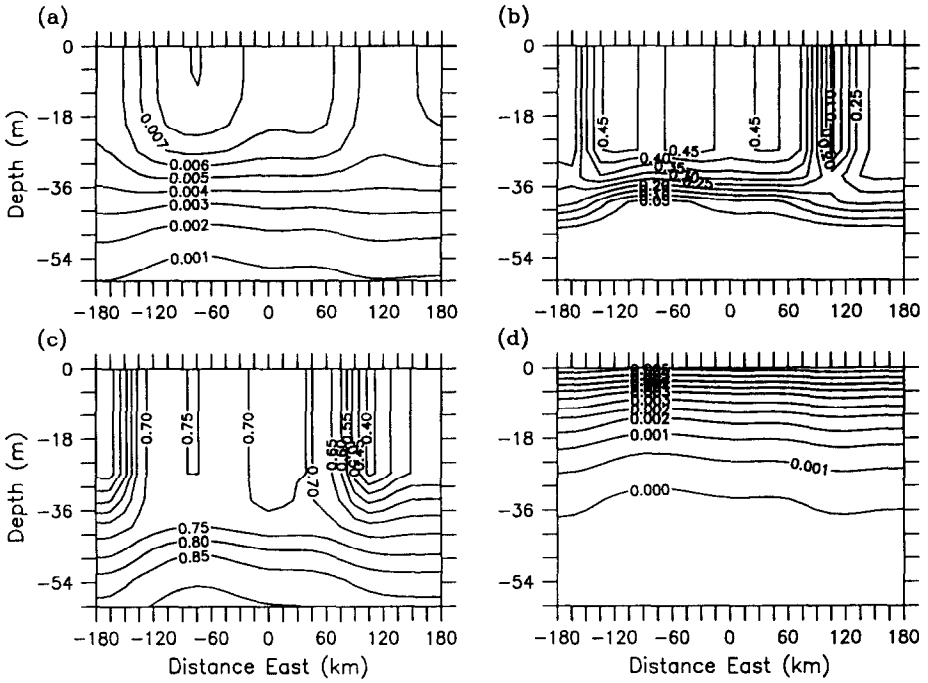

Fig. 17. Vertical sections of (a) primary production ($gNO_3/m^2/day$), (b) *f*-ratio (nondimensional), (c) nutrient limitation factor Q (nondimensional) and (d) photosynthetically available radiation ($cal/cm^2/s$) from west to east across the Small eddy along the line indicated in Fig. 11 on day 180.

It is important to note that this nutrient enhancement causes the three dimensional simulation to appear less consistent with the data inside the eddy on days 142–151 than the one dimensional simulation. There are two possible explanations for this discrepancy. If three dimensional eddy processes were actively transporting nutrients toward the surface in the real ocean during this time, the biological model may have been improperly tuned in MMR95 to counterbalance the absence of these processes in the one dimensional model. Alternatively, it may be that eddy upwelling was not actually taking place inside the eddy on days 142–151 in the real ocean. These mesoscale dynamical events are spatially and temporally intermittent, and the physical oceanographic data available for this experiment are insufficient to determine whether or not upwelling was taking place during this particular time at this location. Therefore it is not possible to ascertain which of these two explanations is more likely.

The time series in Fig. 20 is useful for interpretation of some aspects of the spatial and temporal variability of the data. Previously it has been argued (MMR95) that the drawdown of nitrate in the first time series outside the small eddy was biased by the sampling pattern which covered some cold submesoscale features and then moved toward the interior of the small eddy later in the record. The fact that the data are bracketed by the model solutions inside versus outside the eddy lends plausibility to this argument that spatial variability can be misinterpreted as temporal variability if time series sampling is not conducted in a single water mass. Further analysis of this issue follows in section 7.

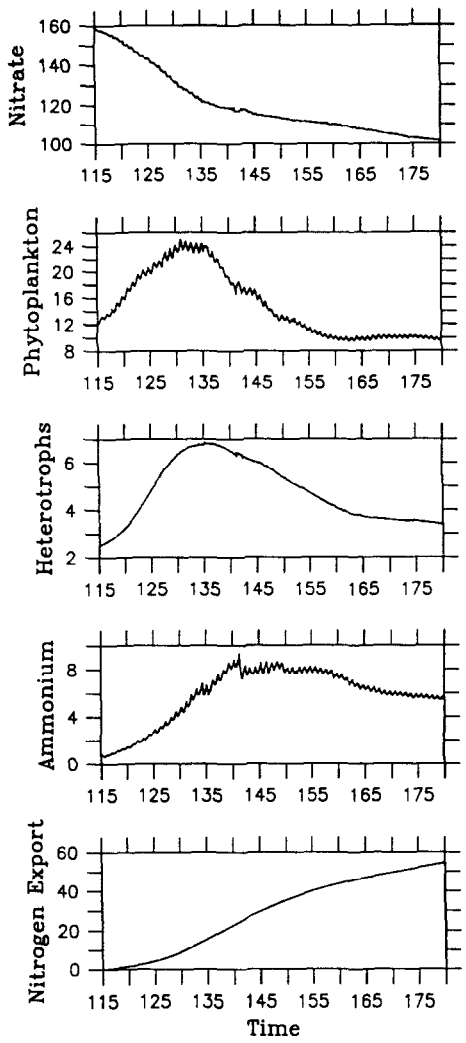

Fig. 19. Time series of the spatially integrated nitrogen reservoirs.

6. THREE DIMENSIONAL SIMULATION: BIG, STANDARD AND SMALL EDDIES

In this simulation the physical field is initialized with the best estimate of the three eddy configuration observed during the beginning of the 1989 North Atlantic Bloom Experiment. Between days 115 and 151 the three eddies evolve and interact (Fig. 21). The Small eddy has become elliptical in shape, with its semimajor axis oriented northwest–southeast. The northwest corner of the small eddy is interacting strongly with the Standard eddy and some deformation of the Standard eddy vorticity distribution is evident in this region. The Standard eddy is also interacting with the Big eddy. A pronounced vortex filament extends eastward from the northeast quadrant of the Standard eddy toward a lobe that has formed in the southern portion of the Big eddy. The southern lobe of the Big eddy extends far enough south so that it appears to be weakly interacting with the Small eddy. A

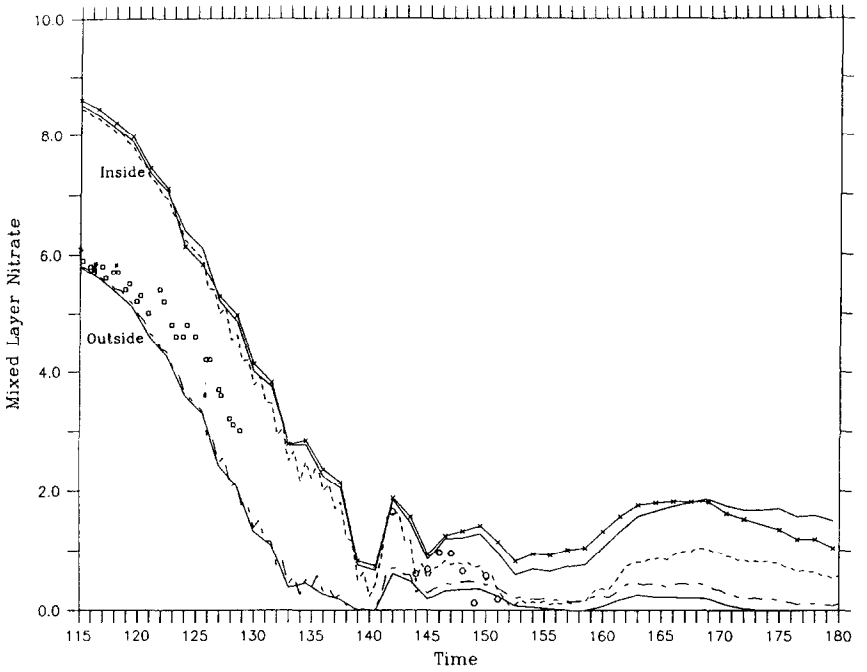

Fig. 20. Time series of mixed layer nitrate concentration (μM) extracted from three dimensional model solutions of the Small eddy in isolation (solid lines) and one dimensional model solutions (dashed lines) inside and outside the small eddy. The solid line connecting crosses corresponds to the time series inside the Small eddy in the three eddy case. Observations are indicated by squares and circles.

submesoscale circulation cell has formed in the center of the three way interaction region (area C on day 151 in Fig. 21). The variations in vertical velocity are associated with the major eddy interactions. The strongest patches of w on day 151 are alternating areas of upwelling and downwelling arranged in east–west streaks in the Standard–Big eddy interaction region. North–south streaks of w are located where the Standard and Small eddies are interacting. Weak patches of w oriented east–west are visible where the southern lobe of the Big eddy meets the Small eddy. The top density pattern is very similar to the vorticity distribution.

By day 151, most of the nitrate has been removed from the mixed layer (Fig. 22). Phytoplankton and heterotrophic biomass distributions reflect the pattern of the initial nitrate field, as the increased availability of nitrate inside the eddies has allowed the bloom to proceed much further there. Advection by the eddy velocities has caused the evolution of asymmetries in the biological fields that are very similar to the patterns in the vorticity field. Mixed layer ammonium concentrations are quite low due to phytoplankton uptake, but show the same pattern on enhancement inside the eddy because the increased biomass has resulted in more nutrient recycling.

One interesting aspect of the biological model solutions on day 151 is the significant enhancement of surface nitrate in the core of the Small eddy. This increase in nitrate appears to be associated with the interaction of the Small and Standard eddies. On day 139, the Small eddy is still mostly circular in shape (Fig. 23a). At this time the maximum

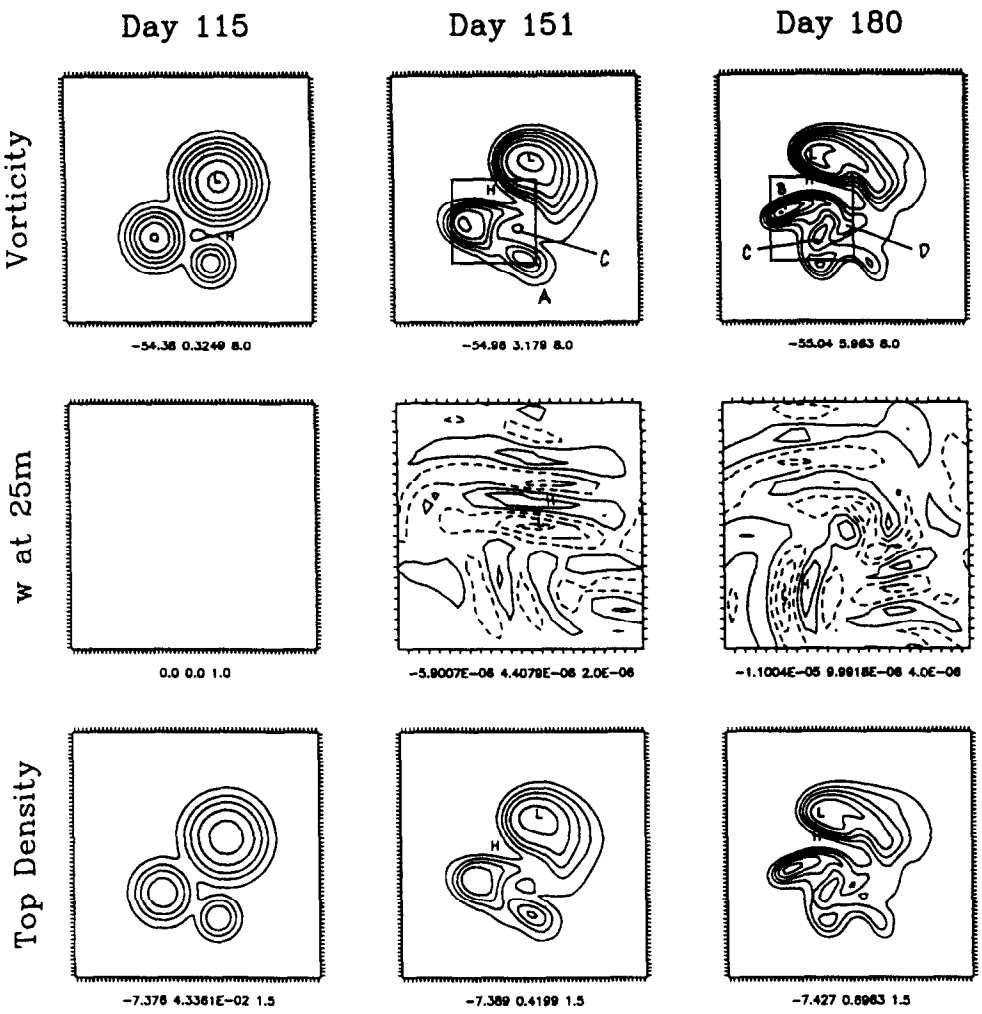

Fig. 21. Maps of vorticity at 50 m (nondimensional), vertical velocity at 25 m (m/s) and top density $\Gamma^2\sigma\psi_z|_{z=0}$ (nondimensional) in the initial condition (day 115) and after 36 and 65 days of integration. Vertical velocity is shown for the inset area indicated on the vorticity maps. Note that the contours on the vorticity and top density maps are negative; the usual convention of using dashed contours for negative values has been omitted in these cases for clarity of presentation.

mixed layer nitrate value is located in the core of the Big eddy (not shown), reflecting the initial nitrate distribution. Between days 139 and 151 the Small eddy becomes demonstrably more elliptic (Fig. 23b). This change in the eddy configuration is accompanied by significant upward displacement of the nitrate surfaces (Fig. 23c). The upwelling of the nutrient surfaces is quite evident in the deeper portions of the vertical section, as displacements as large as 18 m occur along the southeastern edge of the eddy during the 12 day period. Changes in the nutrient surfaces over time are more difficult to diagnose in the euphotic zone for a variety of reasons. First, phytoplankton uptake tends to displace the surfaces downward, countering the upwelling. Further, nitrate removal varies rapidly with

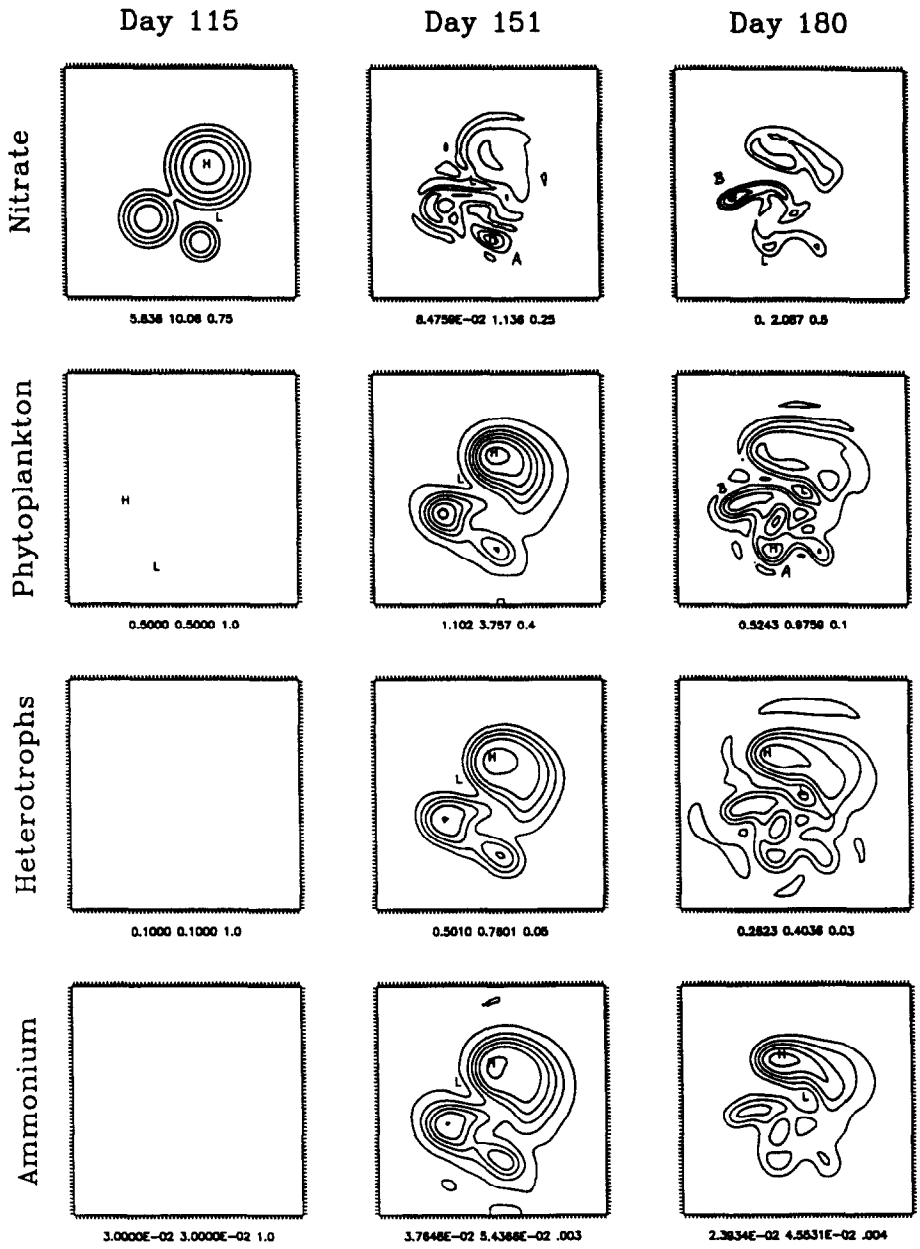

Fig. 22. Maps of mixed layer nitrate, phytoplankton, heterotrophs and ammonium (μM) in the initial condition (day 115) and after 36 and 65 days of integration.

depth because of the exponential extinction of light. Thus the relative strength of the supply and demand processes changes with depth. This is further complicated by the existence of a mixed layer at the surface, in which changes over time reflect the balance between the two processes integrated over the layer depth. Quantitative diagnosis of the model solutions in such circumstances requires a consistent analysis scheme in which the

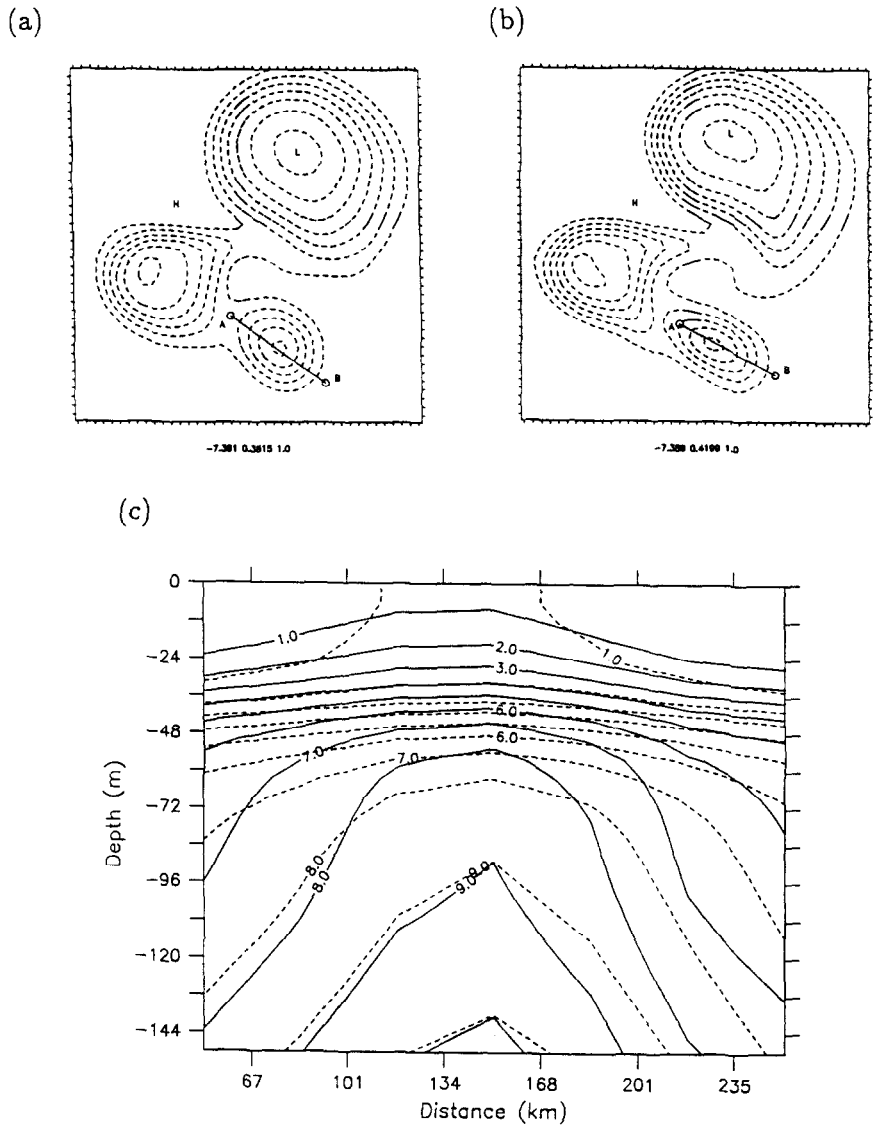

Fig. 23. Maps of nondimensional top density $\Gamma^2 \sigma \psi_z|_{z=0}$ on (a) day 139 and (b) day 151. Panel (c) shows a vertical section of nitrate taken from A to B on day 151 (dashed contours) overlaid on the section taken on day 139 (solid contours).

balance of terms can be examined. However, it is qualitatively clear that the net supply of nitrate from below is responsible for the enhancement of mixed layer nitrate inside the eddy as the 1 μM nitrate surface outcrops on day 151 where it previously did not.

Between days 151 and 180 further evolution and interaction of the three eddies occurs (Fig. 21). The Small eddy separates into two distinct lobes oriented east–west. This configuration is consistent with the eddy structure indicated in the second eddy report documented in Robinson *et al.* (1993). The Standard eddy has become much more elliptical and is interacting very strongly with the western lobe of the Small eddy. The Big

eddy has also become more elliptical and propagated to the west–northwest. Its southern lobe has developed and rotated counter clockwise around the center of the eddy and lies northeast of its previous position on day 151. The interaction feature located at C on day 151 has been swept into the region between the Standard eddy and the western lobe of the Small eddy. An additional interaction feature is now located at D on day 180 that formed as the easternmost filament of the Standard eddy (located just to the north of C on day 151) snapped off. The vertical velocity field is similar in character to that of day 151. The most intense vertical motion is occurring in north–south streaks in the region where the Small and Standard eddies are interacting. East–west streaks are also visible in the neck region between the two lobes of the Small eddy. Alternating patches of upwelling and downwelling also occur in the regions of the strongest vorticity gradients between the Standard and Big eddies.

In general the simulated behavior of the three eddy configuration beyond the time period analyzed in Robinson *et al.* (1993) is consistent with Geosat observations. Analysis of the 14 altimetric tracks that cross the eddy features during the two subsequent repeat cycles (days 145–161 and 162–178) reveals that the features persist and interact during this time period. There is evidence of a deepening of the Standard eddy's sea surface depression associated with its evolution and interaction with nearby features. Although the detailed interaction of the eddies is difficult to ascertain from a subjective analysis of the Geosat tracks alone, the simulated evolution appears consistent with the available data.

In general it is of considerable interest to assimilate the altimetric, hydrographic and biogeochemical data directly into the numerical model to produce optimal estimates of the four dimensional fields as they evolve. This is accomplished by first tuning and validating the model with the data as done here and then directly assimilating it. Such representations will agree with observations where they are available and be dynamically consistent across data sparse regions. Existing methodologies are capable of achieving such a goal and will be used in the near future.

The eddy dynamics has had a remarkable impact on the chemical and biological fields during this period (Fig. 22). Nitrate concentrations inside the Standard eddy on day 180 (location B) have been enhanced to over 2 μM, representing a 10-*fold increase over the background concentration*. This nutrient injection occurs during the period in which the Standard eddy undergoes rapid and dramatic evolution. On day 153, the top density perturbation of the Standard eddy is fairly circular, although its northeast and southeast corners are distorted due to interactions with the Big and Small eddies, respectively (Fig. 24a). The density perturbation at the core is notably diffuse. By day 180, the eddy has become quite elliptical (Fig. 24b). The gradients around its borders have tightened, and the peak perturbation in the eddy core has deepened and become quite sharp. This has a major effect on the nitrate field. Comparing the vertical sections across the Standard eddy on days 153 and 180 shows that the eddy interactions have lifted the deeper nitrate surfaces in excess of 20 m in some locations during this seven day period (Fig. 24c). As before, biological removal damps the effect in the euphotic zone. However, both the 1 μM and 2 μM nutrient surfaces outcrop in an area where mixed layer nitrate concentrations were approximately 0.2 μM before. This flux of nitrate has stimulated phytoplankton growth and resulted in some accumulation in region B in Fig. 22. The maximum phytoplankton concentration is actually located at A, which is the result of the dynamically induced nutrient enhancement in the Small eddy shown at location A on day 151. As with the single

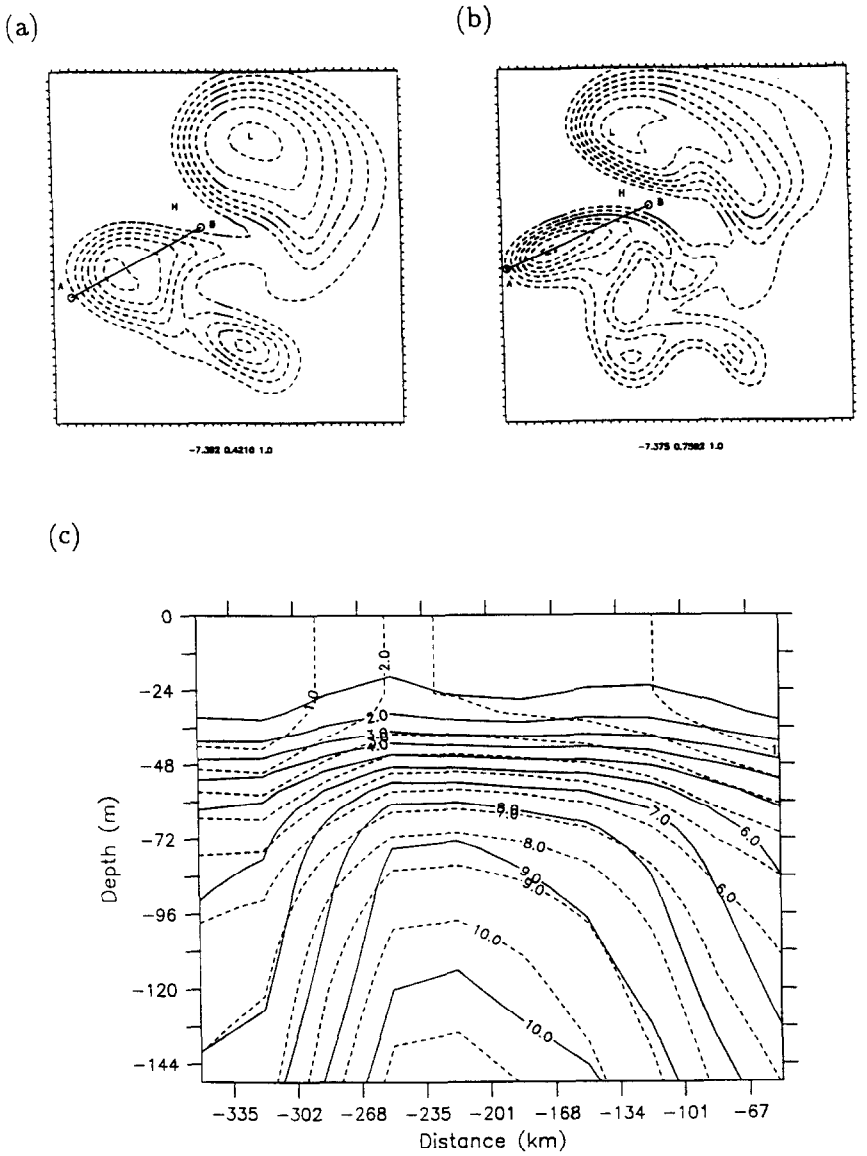

Fig. 24. Maps of nondimensional top density $\Gamma^2\sigma\psi_z|_{z=0}$ on (a) day 173 and (b) day 180. Panel (c) shows a vertical section of nitrate taken from A to B on day 180 (dashed contours) overlaid on the section taken on day 173 (solid contours).

eddy case phytoplankton accumulation is not a strong indicator of primary productivity because the tightly coupled heterotrophic community rapidly consumes excess phytoplankton biomass.

Comparing the Small eddy behavior to the previous case in which it evolved in isolation is instructive. The evolution of the nitrate profile in the core of the eddy is quite different in the two cases (Fig. 25). In the three eddy case the Small eddy begins to separate into the two lobe feature by about day 160. This causes a significant weakening of the eddy pertur-

bation, and the deep nitrate surfaces in the three eddy case take a dramatic turn downward. This behavior is of course not observed in the isolated eddy case as the deep nitrate surfaces continue to rise throughout the simulation. In the mixed layer, nitrate concentrations are quite similar in the two cases until about day 148 when the interaction with the Standard eddy enhances nitrate in the three eddy case (Fig. 20). On day 169 mixed layer nitrate in the three eddy case drops below that of the one eddy case. This is most likely due to two contributing factors. First, the tendency of the Small eddy to propagate to the northwest is not encumbered by the presence of the other eddies in the isolated case. Thus the propagation flux in the isolated case is higher and this enriches mixed layer nitrate concentrations. Second, as the Small eddy separates into two lobes the eddy perturbation decreases, lowering nitrate concentrations.

In general the patterns simulated in the three eddy case are consistent with what few measurements are available concerning the spatial variability of the biological and chemical fields. Airborne Oceanographic Lida (AOL) was used on board the NASA P-3 aircraft during the NABE to observe laser induced chlorophyll fluorescence as a proxy for phytoplankton biomass (Yoder *et al.*, 1993). Structure–function analysis of several overflights of the experimental area revealed alongtrack chlorophyll length scales ranging from 10 km to 290 km. These smallest length scales could be associated with submesoscale features, while the largest scales are consistent with the simulated mesoscale pigment variations. Similar length scales are evident in structure function analysis of Coastal Zone Color Scanner imagery for the region (Robinson *et al.*, 1993). An AOL flight track across the Standard eddy showed enhanced pigment concentrations in the interior of the feature (Robinson *et al.*, 1993). This chlorophyll enhancement was also observed in a SeaSoar survey (Lochte *et al.*, 1993). Chlorophyll concentration inside the eddy was nearly a factor of two higher inside versus outside the eddy, which is consistent with the simulations.

7. A RETROSPECTIVE ANALYSIS OF THE BLOOM DATA WITH THE THREE DIMENSIONAL MODEL

In MMR95 it was argued that the sampling pattern of the early bloom experiment biased the time series by moving from warm features to cold ones. The results of the three eddy simulation lend further support to this claim. Figure 26a shows the cruise track overlayed on a map of mixed layer nitrate concentration extracted from the model on day 128. Sampling began in the interfacial region between the Standard and Small eddies, moved southeast into the swirl of the Small eddy, then southwest away from both eddies, then north toward the swirl of the Standard eddy, and finally a nearly 100 km transit was made back into the swirl of the Small eddy. Recall how the observations are bounded by simulated time series extracted from the model in single water masses inside and outside the Small eddy (Fig. 20). Comparison of early bloom mixed layer nitrate observations with a simulated time series extracted from the evolving model fields along the cruise track shows good agreement (Fig. 26b). The model nitrate drawdown is quite consistent between days 115 and 121 when the observations move from outside the Small eddy into its swirl and back out again. Agreement is also satisfactory from days 127–129 when stations are again located in the swirl of the Small eddy. However, from days 121 to 127 the observations suggest less nitrate removal (more apparent supply) than does the model. While the possibility that the discrepancy is of biological or chemical origin cannot be ruled out, apparent supply from the aliasing of spatial variability is likely. Figure 1 of

(MMR95) shows that the observations during days 121–127 were taken in a distinctively cold water mass to the west of the Small eddy. It may be that this cold feature is a submesoscale flow not represented in the present simulation. Alternatively, the observations could be located in the southeastern flank of the Standard eddy, as Fig. 26a would indicate. If this were the case, a mere 50 km deformation of the Standard eddy in this area (which is well within the error bars of the available data) would provide enough apparent nitrate supply to account for the difference. To demonstrate this, the cruise track is hypothetically extended into the swirl of the Standard eddy (Fig. 26a, dashed line). This brings the resulting time series of mixed layer nitrate into full agreement with the data (Fig. 26b).

In this case it was possible to reconcile the observations with time series extracted from the model simulation. Much more powerful contact between models and data can in general be achieved through the process of data assimilation. Such techniques are routinely used in meteorology and physical oceanography to maintain optimal agreement between observations and models. In fact, data assimilation yields field estimates that agree with the data to within prescribed error bounds and are consistent with model dynamics. Data assimilation schemes will be extremely useful for interdisciplinary applications to maximize the utility of sparse observations in creating dynamically consistent fields that agree with all available data.

8. SUMMARY AND CONCLUSIONS

This study and its companion paper (MMR95) have introduced a mesoscale eddy resolving coupled physical and biological model. The interdisciplinary model system has been tuned to the NABE data in Part 1, and it was shown that the general features of the early phase of the bloom can be represented in a one dimensional framework when the mesoscale spatial variability in the pre-bloom nutrient distribution is treated explicitly. Results from the full three dimensional model indicate that physical structures and transports significantly influence biogeochemical fluxes and ecosystem dynamics. Mesoscale dynamical processes dominate late-bloom and post-bloom biological fields.

The preceding simulations have demonstrated a diversity of mesoscale processes that can transport nutrients into the euphotic zone. Using the nutrient model in an isolated eddy it was possible to isolate and quantify the flux caused by vertical motions arising from various sources. In this case the vertical velocity associated with the internal dynamics of an eddy evolving in isolation is fairly weak, as the flow remains relatively stable and quiescent. The addition of moderate wind forcing more than doubles the nutrient flux through vortex stretching that arises from the advection of the interior vorticity by the Ekman velocity. The effect of these two processes combined accounts for less than half of the total nutrient transport observed when the eddy is allowed to propagate freely. This "propagation flux" causes an effective vertical velocity of approximately 3 m per day in this case. It is the kinematic result of the linear propagation of the domed nitrate surfaces inside the cyclonic eddy. This process is not necessarily limited to vortex propagation. Theoretically this effective upward transport will occur along the leading edge of any moving feature consisting of raised density surfaces. In fact this kinematic mechanism of vertical transport has been identified in the eastward propagation of Gulf Stream meanders and is consistent with RAFOS float observations (Bower, 1991).

Numerical experiments with the full four component biological model provide a more

(a)

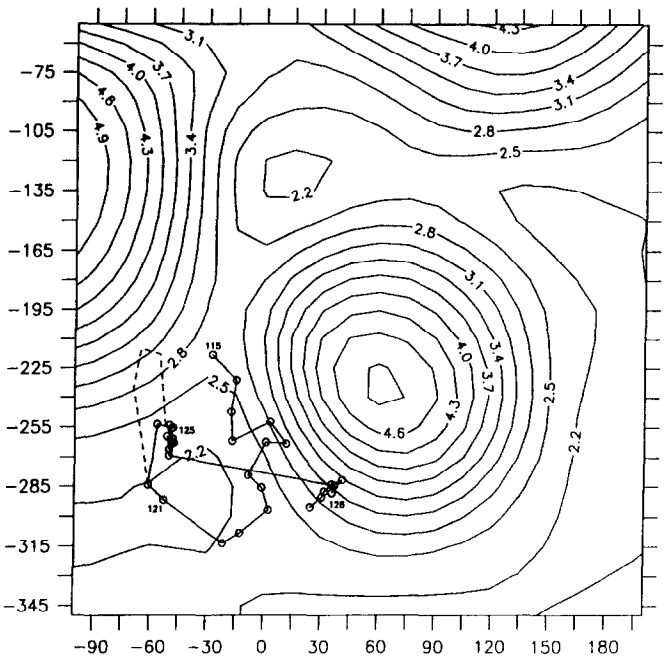
-75
-105
-135
-165
-195
-225
-255
-285
-315
-345
-90 -60 -30 0 30 60 90 120 150 180
3.1
4.0
3.7
4.6
4.3
3.4
2.8
2.5
2.2
115
125
121
128

Day 128.5

(b)

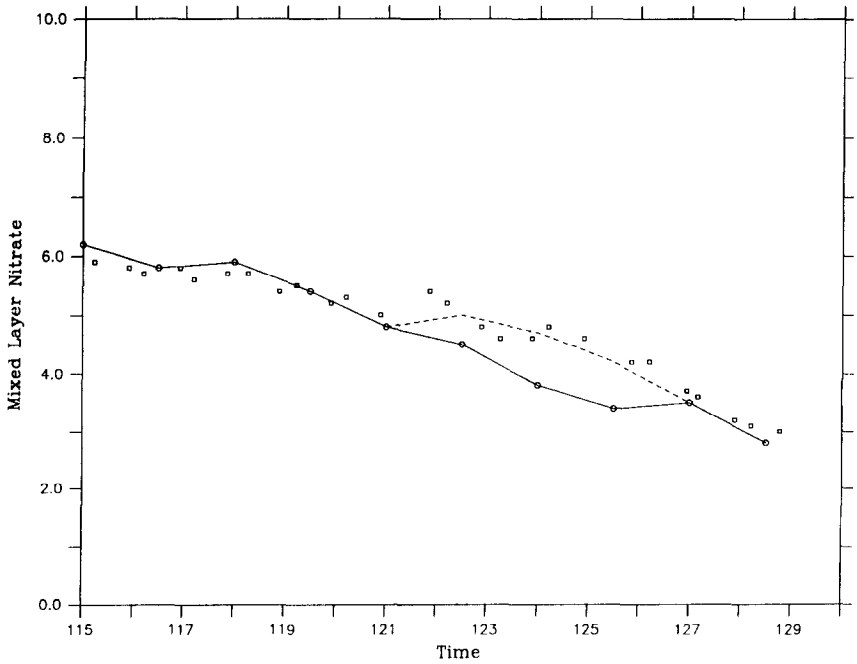
Mixed Layer Nitrate
10.0
8.0
6.0
4.0
2.0
0.0
115 117 119 121 123 125 127 129
Time

realistic context in which the effects of these and other transport processes can be studied. Early in the spring bloom the evolution of the chemical and biological properties of the interior of the Small eddy in isolation is quite similar to that predicted by a one dimensional model. Because the initial condition is well mixed to substantial depth, gradients on which physical transport processes operate are absent in the early part of the simulation. Later in the bloom, after a strong nitracline has been established by phytoplankton uptake, the efficacy of the mesoscale transports begins to emerge. Significant nutrient enhancement is observed in the interior of the vortex which is consistent with the propagation flux. Post-bloom mixed layer nitrate concentrations are more than double those of the one dimensional case. The tightly coupled heterotrophic population damps the phytoplankton biomass response.

In the three eddy case the propagation of the Small eddy is inhibited by the presence of the neighboring vortices. However, the eddy interaction processes in this case turn out to provide a more dramatic nutrient supply to the upper ocean. The Standard–Small eddy interaction pumps even more nitrate into the mixed layer than the free propagation of the Small eddy. This supply of nitrate is converted into phytoplankton biomass and the interior of the Small eddy becomes the biomass maximum in the overall eddy field. A stronger eddy interaction between Standard and Big occurs later in the simulation that results in an order of magnitude enhancement of mixed layer nutrient concentration inside the Standard eddy. This nutrient flux associated with eddy interactions appears to be a general process that occurs over much larger spatial scales (the scales of the eddies themselves) than the submesoscale hotspots predicted by Woods (1988) to be the primary effect of mesoscale dynamics on biological productivity.

Of course the main challenge in fully understanding and unequivocally demonstrating the importance of mesoscale dynamics on biological productivity still remains: that of actually observing intense dynamical events and their biological and chemical ramifications. Recent advances in both remote sensing and *in situ* techniques have made it feasible to sample the relevant variables on appropriate space and time scales. To exploit this observational capability, an interdisciplinary model system such as the one used here can serve as a framework for the synthesis of the extensive and diverse data sets required for capturing coupled physical–biological processes. Assimilation schemes force the model system to stay in agreement with available data and provide dynamically consistent fields across data sparse regions. The availability of these space–time continuous fields facilitates process studies of complex phenomena for which all necessary fields cannot practically be measured. In this regard a synergy is created in the combination of models and data that will greatly accelerate progress toward understanding physical–biological interactions in the world ocean.

Fig. 26. (a) The cruise track (open circles connected by a solid line) overlayed on a map of mixed layer nitrate concentration (μM) extracted from the three eddy simulation on day 128. The year days of selected stations are indicated. The Small eddy is approximately in the center of the domain. Signatures of the Standard and Big eddies appear to the northwest and north of the Small eddy, respectively. The dashed line indicates a hypothetical cruise track (see text). (b) Mixed layer nitrate concentration (μM) observations (squares) and values extracted from the model along the cruise track (open circles connected by a solid line). The dashed line represents the concentration extracted from the model along the hypothetical track shown in panel (a).

Acknowledgements—D.J.M. and A.R.R. were supported by ONR N00014-84-C-0461, N00014-90-J-1593 and N00014-93-1-0577. D.J.M. was also supported by an Office of Naval Research Graduate Fellowship and a VCAR Postdoctoral Modeling Fellowship. J.J.M. was supported by NSF OCE88-17830. Many of the simulations in this study were carried out at the San Diego Supercomputer Center under grants HVD200 and HVD204. The helpful comments of four anonymous reviewers are greatly appreciated.

REFERENCES

Angel M. and M. J. R. Fasham (1983) Eddies and biological processes. In: *Eddies in Marine Science*, A. Robinson, editor, Springer, Berlin, Chapter 22.

Bower A. (1991) A simple kinematic mechanism for mixing fluid parcels across a meandering jet. *Journal of Physical Oceanography*, **21**, 173–180.

Fasham M., H. W. Ducklow and S. M. McKelvie (1990) A nitrogen-based model of plankton dynamics in the oceanic mixed layer. *Journal of Marine Research*, **48**, 591–639.

Flierl G. and C. S. Davis (1993) Biological effects of Gulf Stream meandering. *Journal of Marine Research*, **51**, 529–560.

Franks P., J. S. Wroblewski and G. R. Flierl (1986) Prediction of phytoplankton growth in response to the frictional decay of a warm-core ring. *Journal of Geophysical Research*, **91**, 7603–7610.

Klein P. and B. L. Hua (1988) Mesoscale heterogeneity of the wind-driven mixed layer: influence of a quasigeostrophic flow. *Journal of Marine Research*, **46**, 495–525.

List R., editor (1951) *Smithsonian Meteorological Tables*. Smithsonian Institution, Washington.

Lochte K., H. W. Ducklow, M. J. R. Fasham and C. Stienen (1993) Plankton succession and carbon cycling at 47N, 20W during the JGOFS North Atlantic Bloom Experiment. *Deep-Sea Research II*, **40**, 91–114.

McGillicuddy D., J. J. McCarthy and A. R. Robinson (1995) Coupled physical and biological modeling of the spring bloom in the North Atlantic (I): model formulation and one dimensional bloom processes. *Deep-Sea Research I*, this issue.

McWilliams J. and G. R. Flierl (1979) On the evolution of isolated, nonlinear vortices. *Journal of Physical Oceanography*, **9**, 1155–1182.

Miller D. (1971) Global Atlas of Cloud Cover 1967–1970. Technical report, U.S. Department of Commerce and United States Air Force.

Nelson D., J. J. McCarthy, T. M. Joyce, and H. W. Ducklow (1989) Enhanced near-surface nutrient availability and new production resulting from the frictional decay of a Gulf Stream warm-core ring. *Deep-Sea Research*, **36**, 705–714.

Pollard R. and L. A. Regier (1992) Vorticity and vertical circulation at an ocean front. *Journal of Physical Oceanography*, **22**, 609–625.

Robinson A. (1993) Physical processes, field estimation and interdisciplinary ocean modeling. Reports in Meteorology and Oceanography. Harvard University, Cambridge, MA.

Robinson A. and L. J. Walstad (1987) The Harvard Open Ocean Model: calibration and application to dynamical process, forecasting, and data assimilation studies. *Applied Numerical Mathematics*, **3**(1-2), 89–131.

Robinson A., D. J. McGillicuddy, J. Calman, H. W. Ducklow, M. J. R. Fasham, F. E. Hoge, W. G. Leslie, J. J. McCarthy, S. Podewski, D. L. Porter, G. Saure and J. A. Yoder (1993) Mesoscale and upper ocean variabilities during the 1989 JGOFS bloom study. *Deep-Sea Research II*, **40**, 9–35.

Sarmiento J., R. D. Slater, M. J. R. Fasham, H. W. Ducklow, J. R. Toggweiler and G. T. Evans (1995) A seasonal three dimensional ecosystem model of nitrogen cycling in the North Atlantic euphotic zone. In press.

Strass V. (1992) Chlorophyll patchiness caused by mesoscale upwelling at fronts. *Deep-Sea Research*, **39**, 75–96.

Sverdrup H. (1953) On conditions for the vernal blooming of phytoplankton. *J. Cons. Explor. Mer.*, **18**, 287–295.

Woods J. (1988) Mesoscale upwelling and primary production. In: *Toward a theory on biological–physical interactions in the world ocean*, B. Rothschild, editor, Dordrecht.